Volume 40
DOE/DP40200-102

LLE Review

Quarterly Report

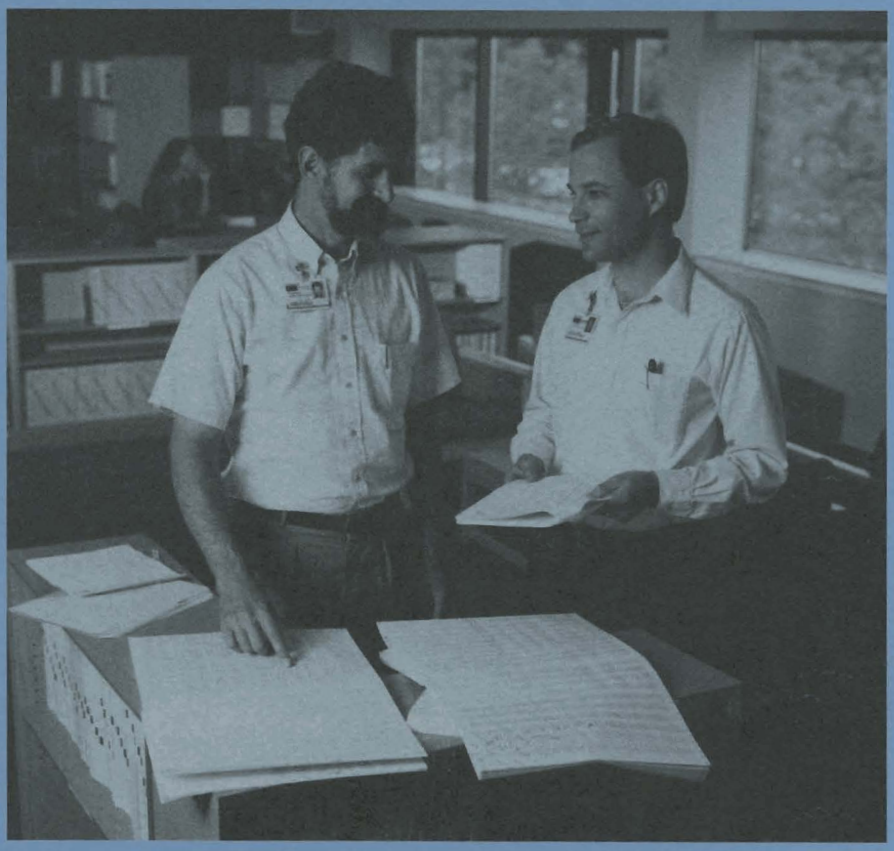

July–September 1989

Laboratory for Laser Energetics
College of Engineering and Applied Science
University of Rochester
250 East River Road
Rochester, New York 14623-1299

Volume 40
DOE/DP40200-102

LLE Review

Quarterly Report

Editor: R. Knox
(716) 275-4366

July–September 1989

Laboratory for Laser Energetics
College of Engineering and Applied Science
University of Rochester
250 East River Road
Rochester, New York 14623-1299

IN BRIEF

This volume of the LLE Review, covering the period July–September 1989, is concerned primarily with uniformity studies. The first article is a report on a series of target experiments with improved irradiation uniformity in which major increases in neutron yields were produced. The first of two articles on theoretical developments presents a new interpretation of burn-through experiments, continuing a study reported in LLE Review 35. The second theoretical article suggests a change in distributed phase-plate design that can improve beam uniformity over that achieved with random-pattern plates. The fourth and fifth articles report that uniformity in the deposition of DT layers in microballoons at very low temperatures has been achieved by a temperature-gradient technique, and that aberration-free interferograms are now being obtained in the target chamber. Finally, the activities of the National Laser Users Facility and the GDL and OMEGA laser facilities are summarized.

Highlights of the research reported in this issue are

- In a recent series of gas-filled implosion experiments greatly improved neutron yields have been obtained as a result of recent improvements in irradiation uniformity. The observed yields came closer to one-dimensional calculated yields.
- The dependence of burn-through time on the nature of barrier layers has been unexplained despite analysis in terms of hot spots, prepulses, shine-through, filamentation, and self-focusing. It is now reported that the anomalous barrier-layer dependence is potentially

understandable in terms of the Rayleigh-Taylor instability, which may mix signature-layer material with the parylene coating.

- Randomly distributed elements may not be the optimum pattern for improving illumination uniformity by distributed phase plates (DPP's). It has been shown in theory that useful improvement in uniformity could result from the reduction of spatial correlations between elements.
- Using a thermal-gradient technique, uniformity of DT target fuel layers has been produced in a transient state. This development is a major step toward the deployment of targets at low temperatures without a beam-blocking cryogenic shroud. Uniformity is achieved in targets at higher pressures than possible with the instant-refreeze technique currently in use.
- With a newly developed achromatic shearing interferometer, aberration-free target interferograms can be made. Two of the new interferometers have been implemented on the OMEGA target chamber to provide orthogonal views. They are remotely controlled for focus, shadowgram shuttering, and tilt and phase adjustment.

CONTENTS

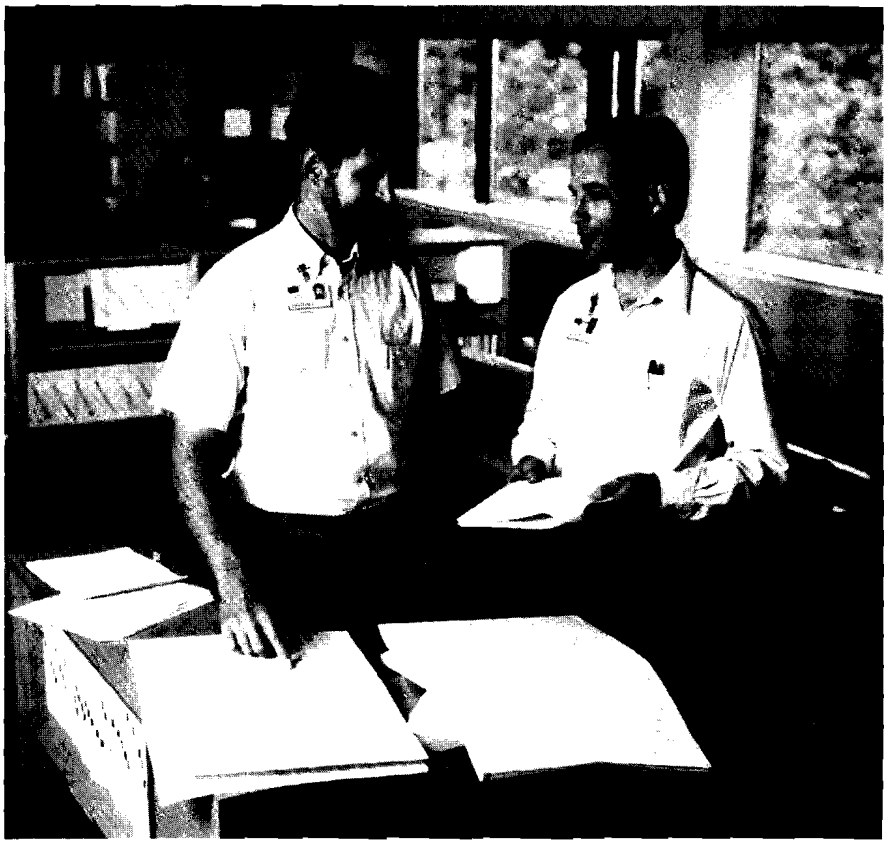

Jacques Delettrez and Reuben Epstein, scientists from the Theory and Computation Group, are shown examining simulation results in the newly expanded library on the second floor of the 1988 Laboratory addition.

Section 1
PROGRESS IN LASER FUSION

1.A Recent Gas-Filled Implosion Experiments on OMEGA

Several experimental campaigns have been successfully carried out on OMEGA since the 24-beam UV system was brought on line in 1985. Initial experiments were devoted to thin-walled glass-shell targets filled with low pressures of DT, in order to obtain high yields and check out the system as a whole. Neutron yields of up to 3×10^{11} were obtained, more than a factor of ten higher than had been obtained on the system in the IR. However, the targets performed in a semi-ablative mode, with the glass shell decompressing from radiation preheat as the implosion proceeded, and the use of a low fuel mass resulted in high fuel temperatures but low densities. Although optimum for neutron production at 1–3 kJ, this mode of implosion does not scale adequately with laser energy. Subsequent series of experiments have therefore been devoted to ablative implosions, with thicker glass walls, which yield higher compressed densities. It is the ablative mode of implosion that scales to ignition and high gain, but, unfortunately, it is the ablative mode that is more susceptible to irradiation nonuniformities and hydrodynamic instabilities. Our experiments have therefore concentrated on two key issues: (1) attempting to achieve nearly one-dimensional implosions; and (2) obtaining and diagnosing high densities.

A series of cryogenic experiments has addressed the second of these issues, and resulted in the first direct measurement of high laser-fusion fuel areal density. Compressed DT fuel densities in the range 20–40 g cm^{-3}, i.e., 100–200 times the density of liquid DT, were

achieved, the highest yet attained in direct-drive inertial fusion experiments. These experiments were reported in Refs. 1–3.

In order to investigate the first issue, the conditions required for the attainment of nearly one-dimensional implosions, we have used primarily gas-filled spherical targets that implode ablatively. Indeed, much of the experimental effort on OMEGA from 1986 to 1989 has been devoted to the implosion of these targets, with the primary emphasis being placed on determining the sensitivity of target performance to irradiation nonuniformity. In this article we report results from an extensive series of recent experiments using these targets. We have found that: (a) the yield, expressed as a fraction of the ideal, calculated, one-dimensional yield, decreases with increasing convergence ratio (initial radius divided by final fuel radius); and (b) as a result of the recent improvements in laser uniformity obtained on the OMEGA system, the observed yield has increased to become closer to the one-dimensional calculated yield.

Experimental Conditions

Typical targets for these experiments have been glass shells of wall thickness $\Delta R_0 \sim 3$–6 μm and radius $R_0 \sim 100$–150 μm, filled with D_2 or DT to pressures of 10–100 atm, and irradiated with up to 1.5 kJ of 351-nm light in pulses of $\sim$700-ps duration. These targets are calculated to have relatively modest in-flight aspect ratios ($R/\Delta R \lesssim 30$), and to stagnate with a wide range of convergence ratios depending on the gas pressure and shell thickness. Compressed fuel densities of up to $\sim$50 times liquid density have been demonstrated for these targets. While higher densities have been obtained for cryogenic targets, gas-filled targets are better suited for studying the effects of irradiation nonuniformity because of the greater complexity of the cryogenic system; in particular, possible initial nonuniformities associated with cryogenic fuel layers are avoided.

A comprehensive set of plasma, x-ray, and nuclear diagnostics has been deployed to characterize these implosions and to permit comparison with hydrodynamic code calculations. Emphasis has been placed on those diagnostics that provide information on compressed fuel conditions.[4] The principal diagnostics are neutron dosimetry, neutron time-of-flight spectrometry,[5] shell-areal-density measurement by neutron activation,[6] fuel-areal-density measurement by knock-on ion spectrometry,[7] x-ray microscopy,[8] time-resolved x-ray photography,[9] and, in later experiments, multiframe x-ray photography.[10–12] In addition, some estimates of the fuel areal density were obtained from measurements of the secondary-reaction products of D_2-filled targets.[13–15]

The fraction of laser energy absorbed by the target and the fraction converted into x rays have generally been found to be in good agreement with the predictions of the one-dimensional hydrodynamic code *LILAC*, assuming modest ($f = 0.06$) thermal flux inhibition.[16] The absorption fraction is dependent on the thickness of the shell, as well as the incident intensity (which varied between 5×10^{14} and 1.5×10^{15} W/cm^2 in these experiments). As an example, the

absorption fraction for 4-μm-thick glass shells varied from ~65% at 5×10^{14} W/cm^2 to ~55% at 1.5×10^{15} W/cm^2, in agreement with one-dimensional *LILAC* simulations to within ±5% throughout this intensity range. Similar agreement between theory and experiment was also found for absorption and x-ray-conversion fractions, over a broad intensity range, in early 24-beam UV experiments carried out on spherical solid-glass targets.[17]

X-Ray-Framing Camera Images

A greatly improved visualization of the implosion process has been made possible by the recent development of an x-ray-framing camera. This is a pinhole camera outfitted with a fast gating system developed at LLNL[10–12] that provides up to sixteen frames with a temporal resolution of 90 ps. It is filtered to respond to x-ray energies above 1.5 keV; for glass shells the images are dominated by silicon *K*-shell line emission. The spatial resolution of the pinhole camera is 12 μm, although the actual resolution of an individual frame is inevitably degraded somewhat by the motion of the target during the 90-ps time window. An example of an implosion diagnosed with this system is shown in Fig. 40.1, for a 5.1-μm-thick glass shell of initial diameter 250 μm filled with 25 atm of D_2. The target has already partly imploded by the time of the first frame; the bright region of maximum emission corresponds approximately to the outer surface of the glass shell where the density and electron temperature are both high. Formation of the compressed core can clearly be seen in the later frames, and good implosion symmetry is evident. Implosion asymmetries are detected far more readily in such framing-camera images than in time-integrated x-ray pinhole photographs.[11]

Streak Camera Images

The implosion history of the same target was also measured using x-ray streak photography (see Fig. 40.2), with the slit of a streak camera placed across the center of an x-ray pinhole image giving 15-μm spatial resolution. Nonlinearity in the streak speed is measured and corrected for by using a series of 100-ps, 351-nm pulses from the DEL laser passed through an etalon. In order to highlight the structure of the image, which is dominated by core emission at the time of peak implosion, two cycles are used on a nonlinear intensity scale; thus, the x-ray intensity at zero radius ($r = 0$) steadily increases with time up to 0.4 ns, and steadily decreases with radius at 0.4 ns. The solid lines superposed upon the experimental image give the *LILAC* predictions for the radius of maximum emission at each time. (Near stagnation, increasing emission from the fuel core causes this radius to jump to the center of the core.) The relative offset between the calculated and experimental time axes has been adjusted to provide the best match, since the absolute experimental timing is not known. Very close agreement is seen throughout the implosion phase. After stagnation, however, some disagreement can be perceived: for example, the core is slightly displaced to positive radius, and the disassembly trajectory for $r > 0$ agrees better with the code than that for $r < 0$. This data is in accord with the general understanding that the effects of irradiation nonuniformity are manifest primarily at the time of stagnation.

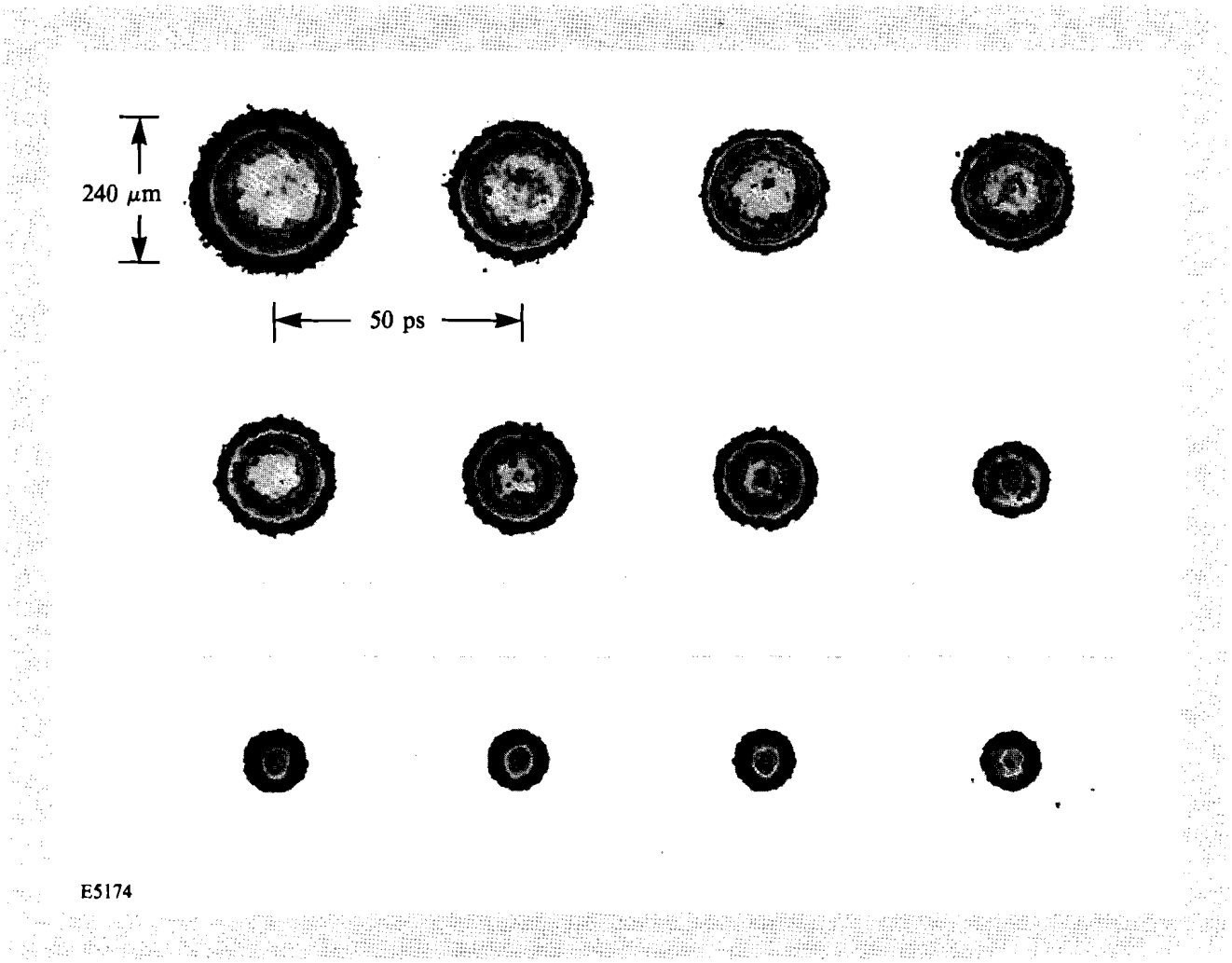

Fig. 40.1
X-ray images of an imploding D_2-filled target taken with a multiframe gated intensifier system coupled to an x-ray pinhole camera.

The conditions at stagnation become hard to resolve when the predicted core size becomes comparable to the resolution of the pinhole camera. With the proposed OMEGA Upgrade, greatly improved diagnosis of the crucial stagnation phase will be possible: the targets will scale to about three times their present diameter, and the ratio of the initial diameter to the smallest resolvable feature in the compressed core will increase by approximately the same factor. In addition, to improve diagnosis of the compressed core, we plan to implement an x-ray microscope with sub-5-μm system resolution in front of the framing and streak cameras.

Target Performance

Since a wide variety of targets has been shot in these experiments, we have found it convenient to measure the target performance in relation to the ideal, calculated, one-dimensional yield. The yield, normalized in this way, is plotted as a function of calculated

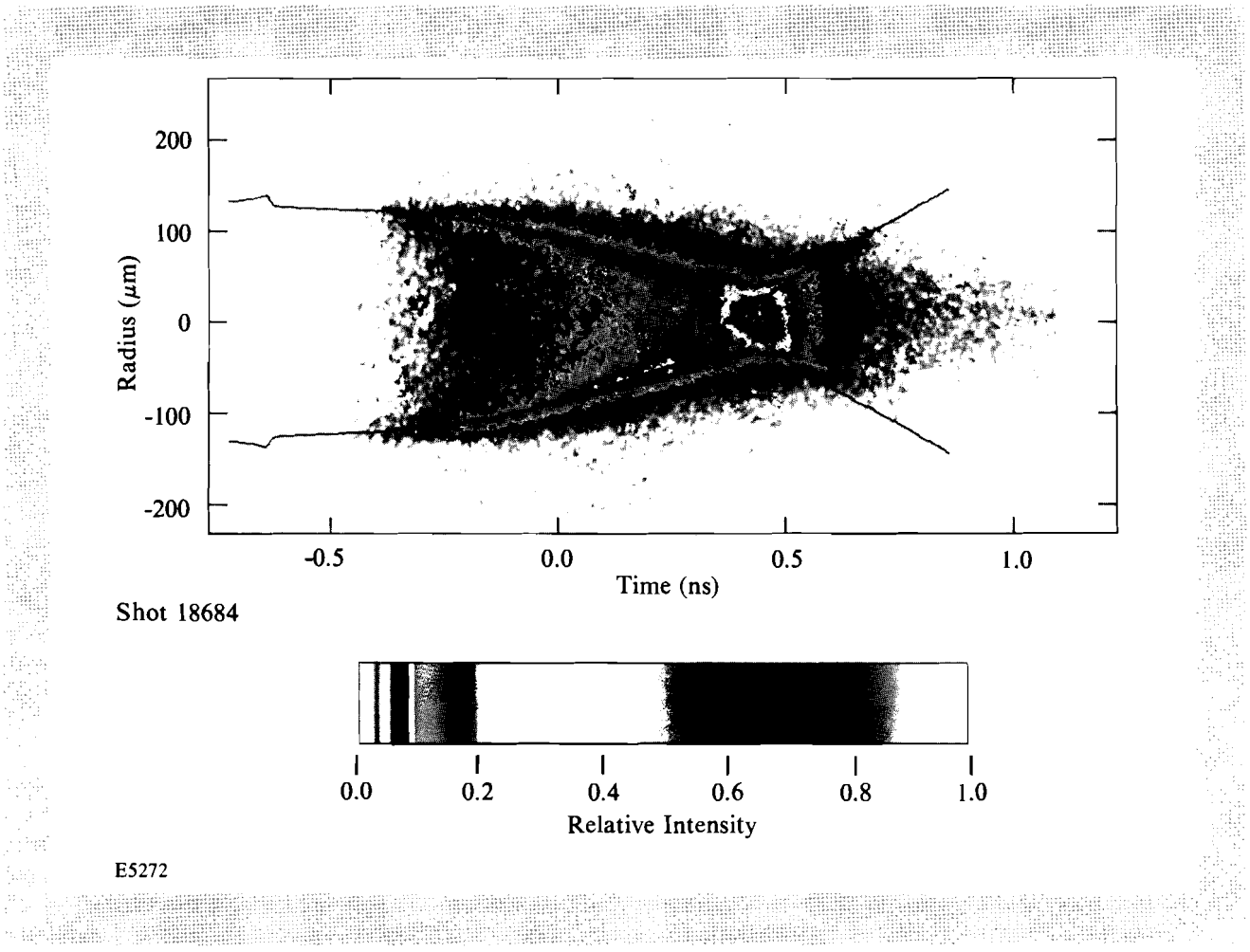

Fig. 40.2
Implosion history of a D_2-filled target recorded by an x-ray imaging streak camera. The trajectory of maximum x-ray emission calculated using *LILAC* is superposed (solid line).

convergence ratio in Fig. 40.3, for targets with shell thickness in the range 2.5–3.5 μm. The open circles correspond to data taken before the implementation of the uniformity improvements on OMEGA (including phase conversion,[18] SSD,[19-21] and beam energy and power balance[22]). The solid circles correspond to 1989 shots on the improved OMEGA laser, mostly with SSD. In both sets of data it is seen that targets that stagnate with fairly large core sizes ($\gtrsim 30$ μm, or convergence ratio $\lesssim 10$) produce near to one-dimensional yields; these targets maintain good symmetry throughout the implosion. However, as the expected convergence ratio of the target increases, the measured yield is degraded.

The most notable feature of Fig. 40.3 is the dramatic improvement seen between the early experiments of 1986 and the more recent experiments of this year. Qualitatively similar results have been obtained for other ranges of wall thickness. Much of the scatter is due to the range of target parameters and laser conditions represented in the figure. In order to examine more quantitatively the effect of SSD, with factors such as beam quality, beam energy, and power balance held constant, two series of shots were taken in which the only parameter changed was the laser bandwidth. The D_2-filled glass shells

used had a diameter of 250 μm and a shell thickness of 5 μm, and were coated with a thin layer of aluminum (see below); the two series corresponded to fill pressures of 25 atm and 10 atm, which have calculated convergence ratios of 17 and 23, respectively. The normalized yield is plotted as a function of bandwidth in Fig. 40.4. Laser conditions on all shots were comparable, except for one shot (the open box) where an amplifier in the driver line misfired, reducing the total system energy but not affecting the uniformity. Substantial improvements are clearly seen using SSD, by factors of 7 and 4, respectively, for the 25-atm and 10-atm targets.

The apparent lack of further improvement for bandwidths greater than 1 Å is interesting, since theory would predict steady improvement: clearly, the larger the frequency difference between interfering DPP elements, the faster should be the smoothing. One plausible explanation of these observations is suggested by the elliptical beam that is formed from the (hexagonal) DPP elements (see Fig. 37.34 of Ref. 21). At higher bandwidths, more energy is deflected towards the edge of the target and the symmetry of irradiation may be compromised. This problem should be straightforward to resolve using stretched hexagonal phase-plate elements; however, quantification of the improvements obtainable with SSD under a variety of conditions, and optimization of the SSD parameters, merits further experimentation.

The experiments on gas-filled targets have included measurements of secondary-reaction products from D_2-filled microballoons, i.e., secondary protons from D-^{3}He reactions and secondary neutrons from D-T reactions, where the ^{3}He and the tritons are generated from the two primary D-D reactions. These products are detected with activation counters, liquid scintillation counters, a plastic scintillator coupled to a microchannel photomultiplier, and filtered CR-39 track detectors. Ratios of the reaction products can yield information about the fuel temperature and ρR; they also indicate that mix between the shell and the fuel is occurring in these experiments. The error bars associated with these measurements are often large on account of the poor statistics associated with the low reaction-product yields. With the greater energies anticipated for the OMEGA Upgrade, these measurements will provide significantly improved diagnostics of the core conditions.

A number of experiments have also been carried out with thick layers of low-Z polymer (parylene) coated over a 3-μm-thick glass shell. The addition of the polymer should reduce the level of radiative preheat of the fuel, and, depending on the ablator thickness, produce a colder (lower isentrope) implosion leading to higher fuel densities. However, from time-resolved x-ray line spectroscopy of special signature-layer targets,[23,24] we have obtained evidence of anomalous early lightup of inner regions of the shell. This phenomenon is most probably associated with intense hot spots in the beam distribution [although an alternative explanation in terms of the Rayleigh-Taylor instability has recently been proposed (see Article 1.B on p. 173 in this issue)]. Even with SSD, which causes oscillation of the on-target

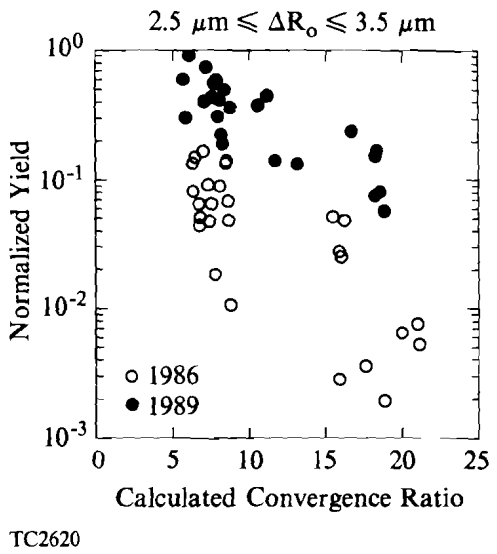

Fig. 40.3
Yield normalized to one-dimensional *LILAC* predictions as a function of calculated convergence ratio, for DT and D_2-filled glass microballoons of various wall thicknesses (2.5–3.5 μm) and fill pressures. Open circles: data taken in 1986 before the implementation of improvements to the irradiation uniformity. Solid circles: data taken in 1989.

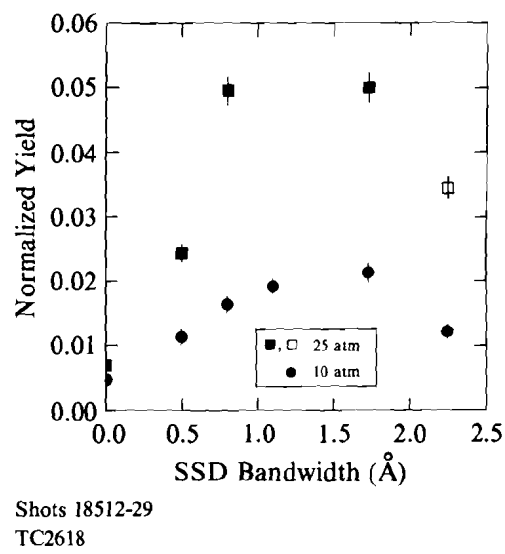

Fig. 40.4
Yield normalized to one-dimensional *LILAC* predictions as a function of the full-width IR bandwidth out of the SSD phase modulator, for 5-μm-thick glass targets of diameter 250 μm containing 10 atm (circles) and 25 atm (squares) of D_2. For all points at each fill pressure, other laser and target parameters were held constant.

hot spots associated with the DPP diffraction pattern (which would be static in the absence of SSD), this effect may not be suppressed, probably because the current modulation frequency of 2.5 GHz is insufficient. However, better target performance has often been obtained (even for glass shells) with the addition of a very thin barrier layer of aluminum to the outside of the target. This phenomenon is not properly understood.

Summary

To summarize these gas-filled implosion experiments, the target hydrodynamics agrees very well with *LILAC* predictions for most of the implosion, but discrepancies are found in the last phases of the implosion around the time of stagnation. This is presumably as a result of irradiation nonuniformities. The core conditions at stagnation are difficult to diagnose, especially for high-convergence-ratio targets, because the core sizes are close to the instrumental resolution limit and secondary-reaction yields are too low at laser energies of ~1 kJ. Improvements in laser uniformity, including SSD, have led to greatly improved target performance for convergence ratios up to 25.

ACKNOWLEDGMENT

This work was supported by the U.S. Department of Energy Office of Inertial Fusion under agreement No. DE-FC03-85DP40200 and by the Laser Fusion Feasibility Project at the Laboratory for Laser Energetics, which has the following sponsors: Empire State Electric Energy Research Corporation, New York State Energy Research and Development Authority, Ontario Hydro, and the University of Rochester. Such support does not imply endorsement of the content by any of the above parties.

REFERENCES

1. R. L. McCrory, J. M. Soures, C. P. Verdon, F. J. Marshall, S. A. Letzring, S. Skupsky, T. J. Kessler, R. L. Kremens, J. P. Knauer, H. Kim, J. Delettrez, R. L. Keck, and D. K. Bradley, *Nature* **335**, 225 (1988).
2. LLE Review **35**, 97 (1988).
3. F. J. Marshall, S. A. Letzring, C. P. Verdon, S. Skupsky, R. L. Keck, J. P. Knauer, R. L. Kremens, D. K. Bradley, T. Kessler, J. Delettrez, H. Kim, J. M. Soures, and R. L. McCrory, to be published in *Phys. Rev. A* (1989).
4. M. C. Richardson, R. L. Keck, S. A. Letzring, R. L. McCrory, P. W. McKenty, D. M. Roback, J. M. Soures, C. P. Verdon, S. M. Lane, and S. G. Prussin, *Rev. Sci. Instrum.* **57**, 1737 (1986).
5. S. A. Letzring, G. Pien, L. M. Goldman, M. C. Richardson, and J. M. Soures, *Rev. Am. Phys. Soc.* **30**, 1481 (1985).
6. E. M. Campbell, W. M. Ploeger, P. H. Lee, and S. M. Lane, *Appl. Phys. Lett.* **36**, 965 (1980).
7. S. Kacenjar, L. M. Goldman, A. Entenberg, and S. Skupsky, *J. Appl. Phys.* **56**, 2027 (1984).
8. M. C. Richardson, G. G. Gregory, R. L. Keck, S. A. Letzring, R. S. Marjoribanks, F. J. Marshall, G. Pien, J. S. Wark, B. Yaakobi, P. D. Goldstone, A. Hauer, G. S. Stradling, F. Ameduri, B. L. Henke, and P. A. Jaanimagi, in *Laser Interaction and Related Plasma Phenomena,* Vol. 7, edited by H. Hora and G. H. Miley (Plenum Press, New York, 1986), p. 179.
9. G. G. Gregory, S. A. Letzring, M. C. Richardson, and C. D. Kiikka, in *High Speed Photography, Videography, and Photonics III,* Vol. 569, (SPIE, Bellingham, WA, 1985), p. 141; G. G. Gregory, P. A. Jaanimagi, P. W. McKenty, S. A. Letzring, and M. C. Richardson, *SPIE* **832**, 383 (1987).
10. J. D. Kilkenny *et al.*, *Rev. Sci. Instrum.* **59**, 1793 (1988).
11. D. K. Bradley, J. Delettrez, P. Jaanimagi, F. J. Marshall, C. P. Verdon, J. D. Kilkenny, and P. E. Bell, in *High Speed Photography, Videography and Photonics VI,* Vol. 981 (SPIE, Bellingham, WA, 1989), p. 176.
12. P. E. Bell, J. D. Kilkenny, G. Power, R. Bonner, and D. K. Bradley, in *Ultra High Speed, High Speed Photography and Videography and Photonics VII* (1989), to be published.

13. E. G. Gamalii, S. Yu. Gus'kov, O. N. Krokhin, and V. B. Rozanov, *JETP Lett.* **21**, 70 (1975).

14. H. Azechi *et al.*, *Appl. Phys. Lett.* **49**, 555 (1986).

15. H. Azechi *et al.*, *Phys. Rev. Lett.* **59**, 2635 (1987).

16. R. C. Malone, R. L. McCrory, and R. L. Morse, *Phys. Rev. Lett.* **34**, 721 (1975).

17. LLE Review **31**, 101 (1987).

18. LLE Review **33**, 1 (1987).

19. S. Skupsky, R. W. Short, T. Kessler, R. S. Craxton, S. Letzring, and J. M. Soures, to be published in *J. Appl. Phys.*

20. LLE Review **37**, 29 (1988).

21. LLE Review **37**, 40 (1988).

22. LLE Review **37**, 16 (1988).

23. J. Delettrez, R. Epstein, M. C. Richardson, P. A. Jaanimagi, and B. L. Henke, *Phys. Rev. A* **36**, 3926 (1987).

24. LLE Review **35**, 113 (1988).

1.B The Role of the Rayleigh-Taylor Instability in Burn-Through Experiments

In a previous LLE review article[1] the results of burn-through experiments with barrier layers carried out on the OMEGA laser system were presented and analyzed. In burn-through experiments, the laser irradiates a spherical target that consists of a glass shell or a solid glass sphere overcoated with a parylene layer in which are embedded one or more thin signature layers of moderate-Z material. The onset time of the characteristic x-ray emission lines from a signature layer is then compared to hydrodynamic code simulations. Barrier layers are thin outer coatings that are deposited over the parylene to prevent the early low-intensity laser light from entering the target. While burn-through experiments were originally conceived to study the thermal transport in laser-fusion targets,[2] they are now directed toward the study of the interaction of light with transparent low-Z materials ($Z < 6$). Low-Z ablators are required for advanced target designs in direct-drive inertial-confinement fusion in order to minimize the radiative preheat of the fuel.[3]

The purpose of the experiments described in Ref. 1 had been to study the effect of barrier layers on the burn-through time. The targets were coated with barrier layers of varying material and thickness: Al, KCl, CsI, and two thicknesses (0.015 μm and 0.05 μm) of Au, and

illuminated by the 24 beams of the OMEGA laser system at 0.351 μm. The simulations were carried out with the one-dimensional hydrodynamic code *LILAC* at nominal intensity (I_0, defined as the laser peak power divided by the initial target radius), and at increasing laser intensities until the simulation burn-through time agreed with the experimental value. The target conditions and the experimental and simulation results are summarized in Table 40.I. The experimental results show that the burn-through times increase with the nuclear Z of the barrier material (except for the KCl case) and that there is a large difference in burn-through time between the bare-parylene target and the aluminum-coated target. In contrast, the simulation results indicate that there is little difference among the burn-through times for all the barrier layers, except for the 0.05-μm gold case, and that the addition of these barrier layers changes the burn-through time by at most 50 ps. The burn-through time itself is not the best quantity for analyzing the results because comparison can only be made between cases with the same target conditions (especially the parylene thickness) and laser parameters (laser intensity and pulse width). A preferable quantity is the laser intensity (I_m) required in the simulations to match the measured burn-through times. In the case of the no-barrier-layer target, large burn-through rates were measured: Laser intensities over ten times nominal are required in simulations to obtain the observed burn-through time. For the Al-barrier-layer target, laser intensities of only three times nominal reproduced the experimental value. For the thick-gold target, only one and a half times nominal intensity is needed to match the observed burn-through times. The KCl case is an exception to the trend: KCl seems to behave partly like parylene and partly like an opaque conductor.

In order to attempt to explain these results, the possibility that the following processes could lead to enhanced burn-through rate was investigated with *LILAC*:

Table 40.I: Onset times of the x-ray emission from the signature layer for the various barrier-layer targets. Tabulated are the measured burn-through times and the simulation burn-through times for increasing laser intensity. All times are with respect to the peak of the pulse. The last column indicates the intensity I_m required in simulations to match the measured burn-through times.

Barrier Layer	Z	Laser Intensity (W/cm^2)	Burn-Through Times (ps)						
				Simulation					
			Measured	1.5 I_o	2 I_o	3 I_o	5 I_o	10 I_o	I_m/I_o
none	–	8.1×10^{14}	−250±20	~400	150	20	−100	−220	12.3±1.3
0.1-μm Al	13	7.5×10^{14}	−25±20	nb	~350(120)	70	−50	−170	4.1±0.4
0.1-μm KCl	18	8.2×10^{14}	−150±20	290	140	30	−80	−180	7.4±0.6
0.1-μm CsI	54	8.0×10^{14}	0±20	~400	160	40	−60	−160	4.1±0.2
0.015-μm Au	79	7.9×10^{14}	125±20	270	140	30	−60	−130	2.1±0.2
0.05-μm Au	79	7.9×10^{14}	350±20	320	210	160	−100	–	1.5

Time in parentheses is for the Al case run with the KCl laser conditions.

TC 2608

- hot-spot intensities exceeding ten times nominal;
- shine-through of the laser light early in the pulse (or a prepulse) while the parylene layer is still transparent;
- a prepulse that would ablate part of the bare-parylene layer; and
- self-focusing of the hot spots and filamentation.

From a detailed analysis[1] of these processes it was concluded that none could explain the experimental results. A brief summary of the reasons is presented here. Hot-spot intensities of ten times nominal in the laser-illumination distribution on target would require hot spots about 40 times nominal in the single-beam distribution because the superposition of the 24 beams of OMEGA smooths out the illumination pattern (at least four beams overlap at any point on the target surface). Yet, both x-ray imaging and equivalent-target-plane imaging do not show the presence of hot spots with such large intensities. Also, the barrier layers are not expected to smooth out the hot spots. Prepulse measurements on the OMEGA laser have led to the conclusion that, if a prepulse existed, its energy would be less than 1 mJ. Such a prepulse cannot ablate enough material to account for the large differences in the burn-through times. As for filamentation and self-focusing, the growth lengths for filamentations are much larger than the electron-density scale lengths prior to the burn-through times. While the growth lengths for ponderomotive self-focusing of hot spots are of the same order as the electron-density scale lengths, it is not expected that barrier layers should affect self-focusing because the growth lengths are independent of Z.

While shine-through alone does not affect the burn-through rate, it can lead to conditions that can enhance the growth of the Rayleigh-Taylor instability, which occurs when a light fluid is accelerated against a heavier fluid and could cause the large, observed burn-through rates by mixing signature-layer material into the parylene layer. Because of its importance, the process will be described in detail and illustrated in Fig. 40.5, where the density and temperature profiles are shown at times of interest. The initial conditions at room temperature are given in Fig. 40.5(a) where the laser comes from the right. Shine-through assumes that, because parylene is transparent to UV light at room temperature,[4] laser light penetrates to the signature layer early in the pulse before breakdown occurs. This process is very attractive because it would explain both the effect of adding a thin barrier layer of aluminum and the difference in burn-through times between the Al and KCl cases. (CsI is also transparent at room temperature, but its use as a photocathode material implies that free electrons can be created very quickly by the laser pulse.) The aluminum layer is thick enough to block most of the laser light early in the pulse (0.1 μm of aluminum has an optical density of about 3.0 for 350-nm light), while KCl seems to behave partly like parylene and partly like an opaque conductor. An opaque barrier layer can prevent prepulses or the early part of the pulse from penetrating into the target and depositing energy inside the target after breakdown has occurred. Breakdown thresholds from high-intensity laser illumination in

parylene and glass are not well known.[5] In the targets used in this experiment, breakdown probably occurs at the parylene-signature-layer interface, especially when the signature layer is an opaque material that absorbs some of the laser light reaching it. This interface can also be the site for impurity deposition during the target-coating process and for target imperfections.[6]

Shine-through was studied using *LILAC* by assuming that, very early in the pulse, the parylene is transparent and absorbs a small fraction of the laser light. At a given intensity threshold, estimated to be about 1×10^{12} W/cm^2 in single-beam shine-through experiments,[4] the breakdown at the interface is modeled by depositing the laser light at the boundary of the parylene and signature layers. The electron temperature increases in the region immediately in front of the deposition region because of thermal conduction. As the parylene ionizes or breaks down, a critical surface is created in that region. Figure 40.5(b) shows conditions in the parylene immediately after the breakdown was initiated. Because it is difficult to model the ionization of parylene at solid density and temperatures below 10 eV, this critical surface cannot be created self-consistently. Instead, the laser light is deposited in the zone where the electron temperature reaches 5 eV (varying this threshold temperature made little difference). This causes an "ionization wave" to propagate quickly from the signature layer toward the target surface [see Fig. 40.5(c)]. At that point, the parylene layer is a slowly expanding plasma with temperatures of a few electron volts and density varying between one-third solid and almost three times solid density. As the laser intensity increases in time, the critical surface reaches the outer surface of the target at about 920 ps before the peak of the pulse [Fig. 40.5(d)]. An ablation surface is established [Fig. 40.5(e)] and the parylene is recompressed. In Fig. 40.5(f), the glass shell is now being compressed by the ablation process. The low-density cavity in the parylene, at the glass-parylene interface, persists until the parylene is completely ablated away. For comparison, the usual development of the ablation front in the absence of shine-through is illustrated in Fig. 40.6. In this case the low-density cavity is much more shallow, and the ratio of the density at the outer glass surface to that of the inner parylene surface is much smaller than for the shine-through case. The one-dimensional burn-through times are not affected much by shine-through because the evolution of the heat front in the initial Lagrangian frame of the materials is not much different in the two cases. However, the nonuniform energy deposition at the parylene-signature-layer interface may lead to a nonuniform low-density plasma in the parylene layer by the time the ablation surface is established. These conditions may seed the Rayleigh-Taylor instability during the implosion, which may lead to a mixing of signature-layer material into the parylene.

We now consider the Rayleigh-Taylor instability in greater detail. The instability can occur in two regions of the target: at the ablation surface and at the parylene-signature-layer interface. Near the ablation surface, the cold, dense shell material is accelerated by the hot, less-dense ablating material during the inward acceleration phase of the

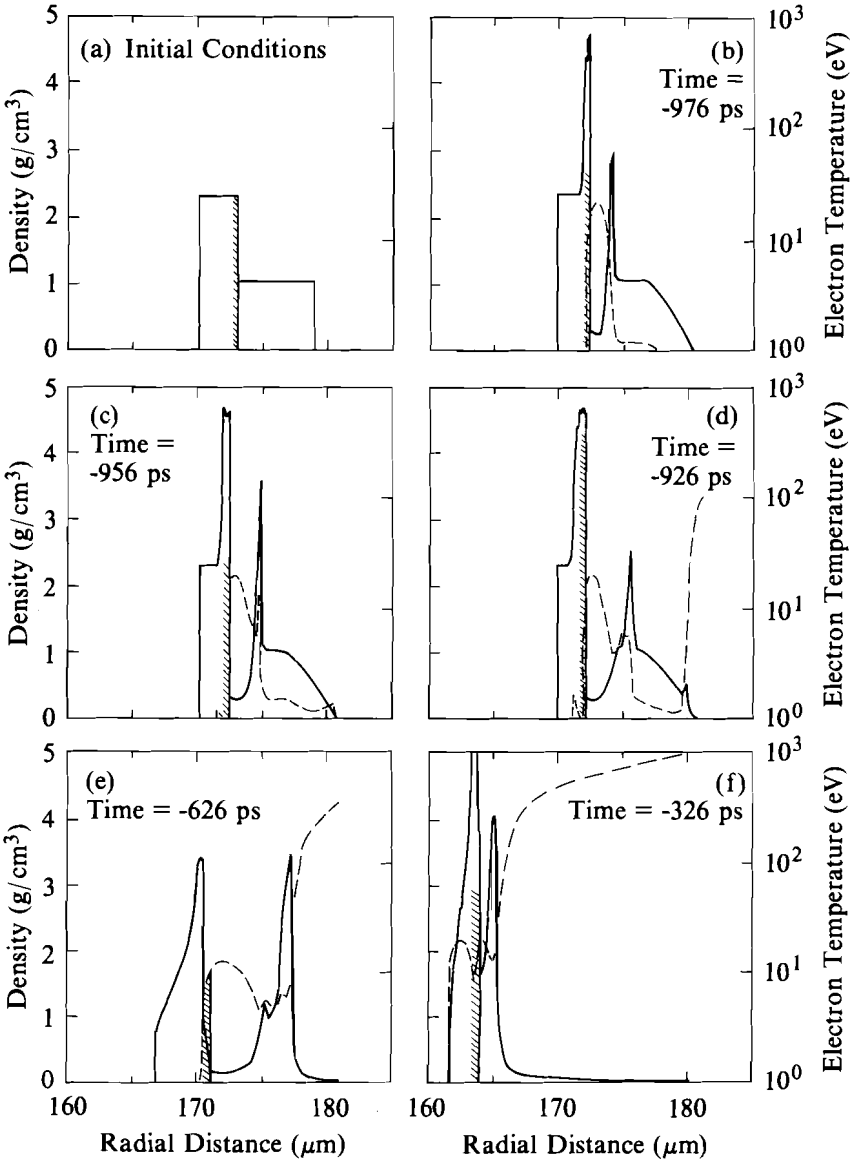

Fig. 40.5
Evolution of the density (solid line) and temperature (dashed line) profiles under shine-through conditions. The target consists of a 3-μm glass shell overcoated with 6 μm of parylene. (a) Initial conditions; the laser comes from the right; (b) 50 ps after the breakdown at the interface; (c) the ionization wave is moving toward the outer surface; (d) the critical surface is established at the outer surface; (e) the parylene is being recompressed by the ablation process; (f) the glass shell is now compressed and is accelerated inward. The low-density cavity in the parylene persists until the parylene is ablated away.

pellet implosion. This situation is analogous to the classical Rayleigh-Taylor fluid instability[7] and is often referred to as the acceleration phase or ablation-surface instability. Numerical simulations have shown, however, that the linear and nonlinear growth rates for the ablation-surface instability are different from those expected from the classical case because they are modified by the ablation process.[8,9] In the burn-through experiments the possible existence of unstable flow development is further complicated by the presence of the unstable interface located at the CH_x-signature-layer boundary, where the lighter parylene is accelerated against the denser signature-layer material. The evolution of this interface is expected to be nearly classical with an Atwood number less than 1. The Atwood number is defined as $[(\rho_H - \rho_L) / (\rho_H + \rho_L)]$, where ρ_H is the density of the heavy fluid (the signature-layer material) and ρ_L is the density of the light fluid (parylene).

The Rayleigh-Taylor instability is analyzed by decomposing the fluid perturbation into Legendre modes. The evolution of the instability is then characterized by the growth rates of these modes. In the references cited above, the growth rates were calculated mostly for single modes. Recently, a number of experimental and theoretical studies[10,11] have shown that the contributions of all potentially unstable modes and their mode-mode interactions must be considered. The treatment of all of these modes, including both their linear and nonlinear evolutions, during the pellet implosion is presently beyond the capabilities of ICF simulation codes. However, models have been developed[11] that estimate the unstable growth and the potential effect of the Rayleigh-Taylor instability on pellet implosions from the zeroth-order (unperturbed) hydrodynamic information obtained from one-dimensional simulations. The evolution of the unstable growth is carried out on a noninterfering basis, i.e., the effect of the instability is not fed back into the one-dimensional simulation.

A model similar to that described in Ref. 11 has been developed to estimate the amount of shell distortion and mixing that could take place during the implosion of burn-through targets. This model computes the modal amplitudes due to the Rayleigh-Taylor unstable flow development and estimates from these amplitudes the mixing region depth $\epsilon\sigma_{\text{rms}}$[11] as a function of time, where ϵ has value of order unity and σ_{rms} is given by

$$\sigma_{\text{rms}} = \left[\frac{1}{4\pi}\sum_{l>1}\sum_{m}|A_{lm}|^2\right]^{1/2} ,$$

where A_{lm} are modal coefficients and the sum is over modes 1 to 200. Linear growth rates for low-Z ablators, which have short density scale lengths, can be expressed as $\gamma = \alpha\sqrt{ka} - \beta k V_a$, where k is the unstable mode wave number; a, the acceleration; and V_a, the ablation velocity given by $\dot{m}/\hat{\rho}$ ($\dot{m}$ is the mass flux rate and $\hat{\rho}$, the peak density).[8,12] The constant values $\alpha \approx 0.90$ and $\beta \approx 3$-4 provide an adequate fit to the growth rates obtained from full two-dimensional

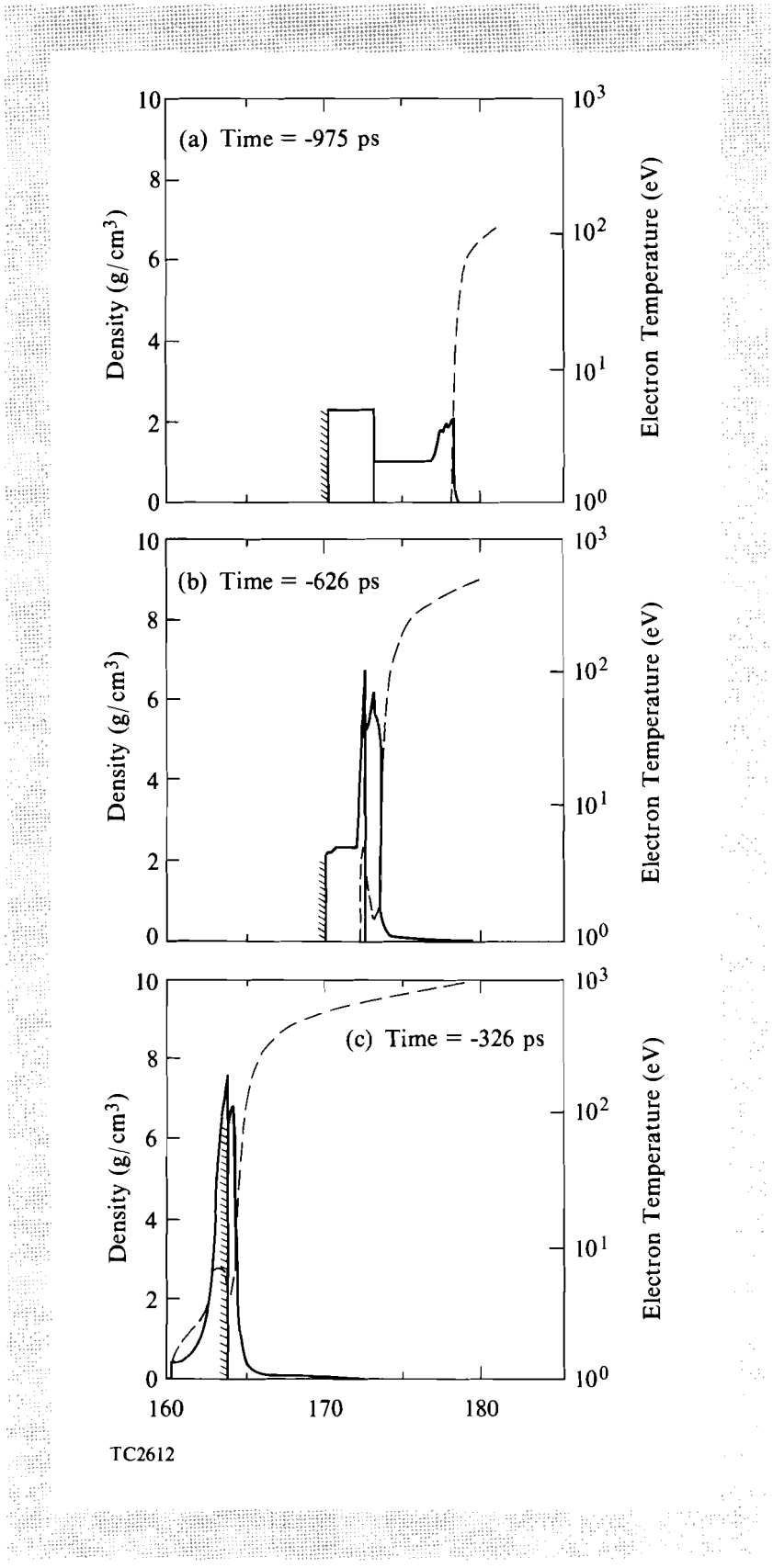

Fig. 40.6
Evolution of the density (solid line) and temperature (dashed line) profiles under the usual simulation conditions. The target is the same as in Fig. 40.5. (a) Laser energy is deposited at the outer surface and the shock wave is compressing the parylene; (b) the shock wave is entering the glass shell; (c) the shell is accelerated inward. The cavity at the interface is shallower than in Fig. 40.5.

simulations over a wide range of initial parameters. Comparisons with growth rates determined by two-dimensional simulations with *ORCHID*[13] for the experiments of interest showed that this expression with $\beta = 3$ gives a reasonable fit. The model tracks the growth of individual modes using the linear growth rates until some saturation amplitude is reached. As the instability evolves, bubbles develop toward the high-density side of the ablation surface and spikes grow toward the outside of the target. In the case of the ablation surface instability, we are interested in the development of the bubble, which has the potential of reaching into the signature layer. After a given mode has reached the nonlinear regime, the amplitude of the bubble (mode) is assumed to continue to grow linearly in time.[14] (Studies have shown that, for finite fluid layers and during the nonlinear evolution, the motion of the bubble departs from constant velocity as the layer thickness gets smaller.[15] However, since this model is used only to illustrate the potential effects of the instability, no attempt has been made to treat the nonlinear stage more accurately.)

The model also calculates the evolution of the parylene-signature-layer interface instability during the implosion. The linear growth rates used for the interface instability are given by $\gamma = \sqrt{Aka\,/\,(kL + 1)}$, where L is the mass-density scale length. In this case we want to estimate to what extent the signature-layer material can penetrate into the parylene layer. We have adopted the spike amplitude suggested in Ref. 11 to estimate the extent of the spike penetration into the ablation region.

In order to obtain an estimate of the mixing-layer depth in burn-through targets, we consider a range of simple initial-amplitude cases. We assume that the laser illumination nonuniformity produces the dominant source of initial-amplitude seeds to the Rayleigh-Taylor instability, which can be represented by $\xi = \xi_0 \exp[-(\Delta R/R)\ell]$ (μm/mode), where ΔR is the separation distance between the ablation and critical surfaces; R, the target radius; and ℓ, the Legendre mode number.[16] For the first case we consider $\Delta R/R = 0.05$ and three values of ξ_0 such that $\sigma_{rms1} = 0.304$ μm, $\sigma_{rms2} = 0.167$ μm, and $\sigma_{rms3} = 0.0304$ μm. For the second case we set $\Delta R/R = 0.01$ and adjust ξ_0 such that the same values of σ_{rms} are obtained. The targets are 3-μm glass shells coated with parylene thicknesses varying from 4 μm to 10 μm and with radii and incident laser intensities similar to those in the experiments described in this article. The simulations were run in the usual absorption mode, without shine-through effects. Figure 40.7 displays an example of the model prediction for the thickness of the mix layers that could potentially be generated by the growth of the Rayleigh-Taylor instability as a function of time for two cases: a 4-μm parylene layer [Fig. 40.7(a)] and a 6-μm parylene layer [Fig. 40.7(b)]. The initial conditions for both cases are $\sigma_{rms} = 0.167$ μm and $\Delta R/R = 0.05$ μm. The solid line is the in-flight thickness of the overdense parylene, defined as the difference between the position of the overdense portion of the target and the position of the parylene-glass interface. The position of the overdense portion of the target is determined by searching for the location of the peak in the density from the outer radius inward and determining the radial location of the

e-fold from the peak density outward. The dashed lines show the increase with time of the thicknesses of the unstable regions associated with the ablation-surface (A) and with the parylene-glass interface (I). For the initial conditions used in this example, the ablation-surface instability has the largest mixing region. No interfacial coupling was assumed between the ablation surface and the parylene-glass interface in order to illustrate the respective evolution of the two unstable regions. If a coupling of the form $\exp(-k\,\Delta R)$,[7] where ΔR is the distance between the two surfaces, was assumed, larger growth would be obtained at the parylene-glass interface.

The signature times, defined as the time of the earliest crossover of either of the dashed curves with the parylene thickness curve, are shown in Fig. 40.8 for parylene thicknesses of 4 to 10 μm. The curves labeled 1, 2, and 3 represent the signature times for the cases with initial amplitude of 0.304 μm, 0.167 μm, and 0.0304 μm, respectively. Figure 40.8(a) is for $\Delta R/R = 0.05$ and Fig. 40.8(b), for $\Delta R/R = 0.01$. The resulting signature times show that, depending on the modal spectrum and amplitudes, the Rayleigh-Taylor instability could grow fast enough to cause the signature-layer material to reach the heat front and emit at the early times observed in the experiments. For example, curve 2 for $\sigma_{rms} = 0.167$ μm in Fig. 40.8(a) yields signature times close to the observed burn-through time for the bare parylene target (-250 ps). The signature times from the mixing model should be used only as an indication because they were obtained with a simplified model of the evolution of the Rayleigh-Taylor instability and were based on a reasonable guess of the amplitude and spectrum of the initial perturbations. The results do indicate, however, that for reasonable rms-perturbation levels, the Rayleigh-Taylor instability could potentially lead to the early mixing of low-Z ablator and signature materials.

The effect of adding different types of barrier layers on the signature times obtained from the mixing model could be explained as follows. Early shine-through can create density perturbations at the parylene-signature-layer interface as was discussed previously and these perturbations can seed the Rayleigh-Taylor instability. The addition of an opaque barrier layer would reduce the amount of shine-through light reaching the interface, thus reducing the initial perturbations and delaying the signature times as shown in Fig. 40.8. For example, while in Fig. 40.8(a) an initial amplitude with $\sigma_{rms} = 0.167$ μm (curve 2) is needed to match the observed burn-through time for the bare-parylene target, the smaller value of 0.0304 μm (curve 3) is required to match the burn-through time of the Al-barrier-layer target. The lower value of initial amplitude could explain the difference in burn-through times between the bare-parylene case and the aluminum-barrier-layer case. As to the effect of adding different types of barrier layers, the various layers would let different amounts of laser light shine through, producing variations in the initial perturbation. For example, KCl is probably more transparent to the laser light than aluminum; thus, the KCl-coated targets would sustain larger initial perturbations than the aluminum-coated target. Also the difference in the burn-through time between the thick-gold case and the thin-gold

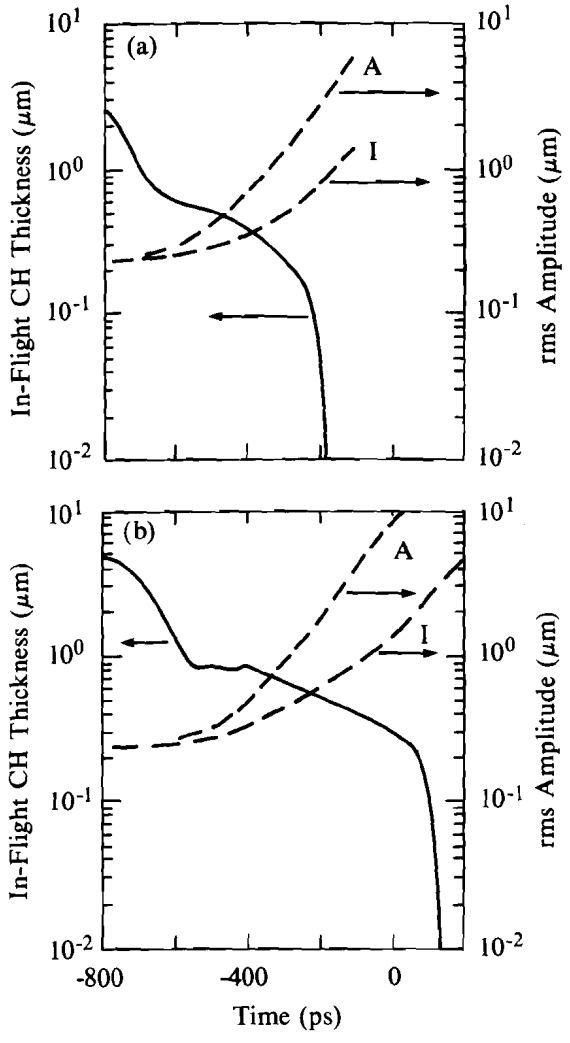

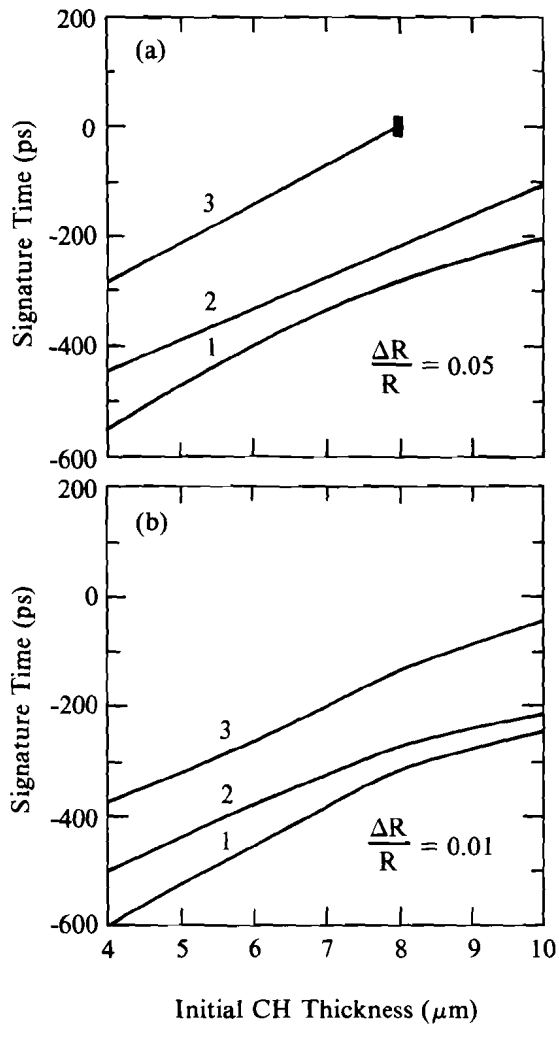

Fig. 40.7
Results of the Rayleigh-Taylor instability mixing model for a glass shell coated with (a) 4 μm of parylene and (b) 6 μm of parylene. The solid line is the temporal evolution of the parylene thickness and the dashed lines the evolution of the thickness of the unstable (mixing) region for the ablation-surface instability (A) and the glass-parylene-interface instability (I). The initial perturbation has a σ_{rms} = 0.167 μm and $\Delta R/R$ = 0.05 in both cases. The earliest crossing of one of the solid lines with the dashed lines is taken as the onset time of emission from the glass shell due to mixing.

Fig. 40.8
Onset time of emission from the glass shell obtained from the mixing model as a function of the parylene thickness for $\Delta R/R$ = 0.05 (a) and 0.01 (b). Curves 1, 2, and 3 are for initial perturbations with σ_{rms} = 0.304 μm, 0.167 μm, and 0.0341 μm, respectively. The solid rectangle at the end of curve 3 for $\Delta R/R$ = 0.05 indicates the signature layer does not mix through the parylene layer for larger thicknesses.

case, which can be partially explained by the *LILAC* simulations from the increase in the amount of gold to be heated and ablated (about 60 ps out of the 225-ps difference), could be due to differences in the early shine-through (the thick-gold layer is more opaque than the thin-gold layer) and by increased radiation preheat from the thick-gold barrier layer, which radiates for a longer time than the thin one. Radiation preheat tends to increase the density gradients in the target, thus reducing the Rayleigh-Taylor growth rate.

The preceding analysis of mixing due to the Rayleigh-Taylor instability may explain the fast burn-through rates observed in the experiment. However, it should be noted that, if the Rayleigh-Taylor instability was present, its effects on the implosion dynamics might not be observable experimentally. *LILAC* simulations of OMEGA gas-filled and cryogenic target implosions[17] show reasonable agreement with experimental observables, such as laser energy absorption, x-ray conversion for moderate-Z materials, implosion velocity, and time of core formation. This indicates that the unperturbed one-dimensional flow obtained by *LILAC* approximates well the gross features of the implosions. Numerical simulations of the development of the nonlinear evolution of Rayleigh-Taylor unstable flow have shown that there exists no large departure in the motion of the centroid of mass of the shell between implosions that are uniform and those that are distorted due to unstable growth.[13] Therefore, if the Rayleigh-Taylor instability was present in the burn-through experiment, it might not be possible to confirm its presence with the usual array of diagnostics deployed during OMEGA experiments.

Summary

We had previously reported on burn-through experiments with barrier layers consisting of different materials and thicknesses that showed burn-through occurring progressively later during the pulse for the following succession of barrier layers: none, aluminum, thin gold, and thick gold. Simulation results had predicted that there should be only small differences ($\sim$50 ps) among the burn-through times of all the barrier layers, except for the thick-gold barrier layer. None of the following processes could adequately explain the experimental results: severe hot spots (intensities ten times nominal), shine-through, the presence of a prepulse, filamentation, and self-focusing. We now have shown that the Rayleigh-Taylor instability has the potential of mixing signature-layer material far enough into the parylene that early-time x-ray emission from the signature layer would be observed. The effect of an opaque barrier layer would be to prevent the target damage caused by shine-through, thus reducing the initial perturbations that seed the instability. Varying the material and the thickness of the barrier layer would affect the shine-through, which would vary the seed of the instability. Since little is known about the transmission and breakdown characteristics of materials to 350-nm laser light at laser intensities below 10^{13} W/cm^2, experiments are planned to understand the shine-through behavior of thin barrier layers. Finally, burn-through-type experiments with improved laser-illumination uniformity could provide qualitative information on the degree of mixing of the signature layer into parylene due to the Rayleigh-Taylor instability.

ACKNOWLEDGMENT

This work was supported by the U.S. Department of Energy Office of Inertial Fusion under agreement No. DE-FC03-85DP40200 and by the Laser Fusion Feasibility Project at the Laboratory for Laser Energetics, which has the following sponsors: Empire State Electric Energy Research Corporation, New York State Energy Research and Development Authority, Ontario Hydro, and the University of Rochester. Such support does not imply endorsement of the content by any of the above parties.

REFERENCES

1. LLE Review **35**, 113 (1988).
2. J. Delettrez, *Can. J. Phys.* **64**, 932 (1986); P. A. Jaanimagi, J. Delettrez, B. L. Henke, and M. C. Richardson, *Phys. Rev. A* **34**, 1322 (1986).
3. LLE Review **23**, 125 (1985).
4. T. Boehly, D. Bradley, and J. Delettrez, paper H6, 19th Annual Anomalous Absorption Conference, Durango, CO (1989).
5. N. Bloembergen, *IEEE J. Quantum Electron.* **QE-10**, 375 (1974); LLE Review **35**, 125 (1988); W. Seka (private communication).
6. H. Kim (private communication).
7. G. Taylor, *Proc. R. Soc. London, Ser. A:* **201**, 192 (1950); D. J. Lewis, *Proc. R. Soc. London, Ser. A:* **202**, 81 (1950); S. Chandrasekhar, *Hydrodynamic and Hydromagnetic Stability*, (Clarendon Press, Oxford, England, 1961), Chap. 10.
8. H. Takabe, K. Mima, L. Montierth, and R. L. Morse, *Phys. Fluids* **28**, 3676 (1985).
9. M. H. Emery, J. H. Gardner, and J. P. Boris, *Phys. Rev. Lett.* **48**, 677 (1982); C. P. Verdon, R. L. McCrory, R. L. Morse, G. R. Baker, D. I. Meiron, and S. A. Orszag, *Phys. Fluids* **25**, 1653 (1982).
10. K. I. Read, *Physica 12d*, 45 (1984); D. L. Youngs, *Physica 12d*, 32 (1984).
11. S. W. Haan, *Phys. Rev. A* **39**, 5812 (1989).
12. S. E. Bodner (private communication); M. Tabak (private communication).
13. *ORCHID* is a two-dimensional Lagrangian hydrodynamic code that is described in some length in Ref. 3.
14. G. Birkhoff and D. Carter, *J. Math. Mech.* **6**, 769 (1957); P. R. Garabedian, *Proc. R. Soc. London, Ser. A:* **241**, 423 (1957).
15. G. R. Baker, D. I. Meiron, and S. A. Orszag, *Phys. Fluids* **23**, 1485 (1980).
16. S. E. Bodner, *J. Fusion Energy* **1**, 221 (1981).
17. R. L. McCrory, J. M. Soures, C. P. Verdon, F. J. Marshall, S. A. Letzring, S. Skupsky, T. J. Kessler, R. L. Kremens, J. P. Knauer, H. Kim, J. Delettrez, R. L. Keck, and D. K. Bradley, *Nature* **335**, 225 (1988).

Section 2
ADVANCED TECHNOLOGY DEVELOPMENTS

2.A Anticipated Improvement in Laser-Beam Uniformity Using Distributed Phase Plates with Quasi-Random Patterns

Distributed phase plates (DPP's)[1,2] have been used at LLE[3] to improve laser-irradiation uniformity on target. We will show that uniformity can be further improved by using DPP's where the spatial correlations in the pattern of phase elements have been reduced, relative to the correlations that would occur fortuitously in random patterns. Diffraction theory[4] shows that the size and wavelength of the nonuniformity are determined by spatial correlations in the phase distribution of the beam. Long-wavelength nonuniformities in the intensity distribution, which are relatively difficult to overcome in the target by thermal smoothing and in the laser by, e.g., spectral dispersion (SSD),[5] result from short-length correlations in the phase distribution of the beam. We have constructed DPP patterns with smaller short-range correlations than would occur randomly. Calculations show that if variations in the intrinsic phase error of a beam over short distances in the aperture plane are sufficiently small, then a "reduced-correlation" DPP will produce a net phase distribution with correlations over these separations that are also less than would occur randomly. As a result, the long-wavelength nonuniformities in single-beam intensity patterns can be reduced with these masks. We will show how the degree of improvement depends on the intrinsic phase error of the beam. We will also show the effect of this improvement on the uniformity of spherical illumination by multibeam systems.

A random two-level DPP is a flat, transparent plate divided into a large number of identical area elements, except that half of them, chosen at random, add a half-wave delay to the transmitted light.[1] At present, the random DPP's on the OMEGA laser system, illustrated in Fig. 40.9, use elements shaped as regular hexagons.[3] Without a DPP, the target is placed within the converging focused beam at the point on the axis where the beam illuminates a full hemisphere. This gives an intensity distribution on target with large, long-scale modulations caused by phase nonuniformities in the beam.[6] With a DPP in the beam as shown in Fig. 40.9, the random phase distribution effectively divides the beam into beamlets that focus onto the target within an area determined by the diffraction limit of the individual mask element. The element size is chosen so that the diffraction-limited focal spot of an individual beamlet matches the target diameter. As evident in Fig. 40.10, the interference among the beamlets produces modulation that is much finer and much more easily smoothed in the target and in the laser itself, e.g., by induced spatial incoherence (ISI)[7] or by SSD.[5]

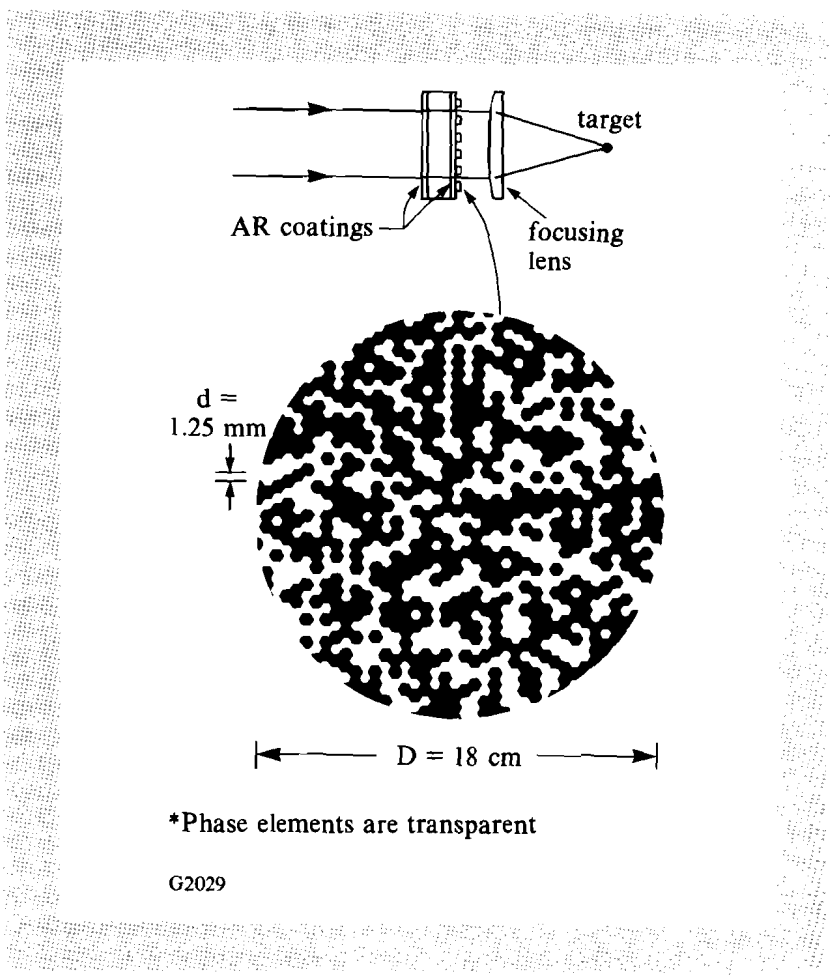

Fig. 40.9
DPP's in current use on the OMEGA laser system are regular arrays of hexagonal area elements, half of which, chosen at random, impart a half-wave phase delay to the passing light.

The functional form of the intensity distribution resulting from using a DPP can be expressed as the smooth, ideally uniform intensity distribution of the individual DPP element, multiplied by a modulating function of the form of a Fourier series with coefficients equal to values of the correlation function of the profile beam's net phase distribution $\phi(\vec{x})$ after passing through the DPP. The oscillations of the modulation function account for the beam nonuniformity, so the uniformity can be improved if the correlation function can be reduced. If the intrinsic phase error of the beam is sufficiently constant over a given distance in the near-field plane, then correlations in the net phase over this distance can be reduced by altering the correlation properties of the DPP. The critical limitation is the phase error in the beam. If it is large, compared with about a quarter wave over a given scale length, then the correlation properties of the DPP over that scale length will be overwhelmed by the intrinsic phase distribution of the beam.

The relationship between the nonuniformity of the focused illumination and the correlation properties of the net phase distribution of the beam can be obtained from the Fraunhofer equation for the diffraction of a signal field $U(\vec{q})$ of total energy E per unit time and wavelength λ irradiating an aperture of area A,

$$U(\vec{q}) = \frac{1}{\lambda R}\sqrt{\frac{E}{A}} \iint_A W(\vec{x})\, e^{-i[\vec{q}\cdot\vec{x} + \phi(\vec{x})]} d^2x \ , \qquad (1a)$$

where $W(\vec{x})$ is the amplitude distribution in the aperture plane, normalized so that

$$\iint_A W^2(\vec{x})\, d^2x = A \ , \qquad (1b)$$

and where $\phi(\vec{x})$ is the sum of the intrinsic phase distribution of the beam plus the phase added by the DPP.[4] The vector $\vec{x}$ is a point in the aperture plane, $\vec{q}$ is the wave vector of the diffracted signal, and R is the distance from the aperture plane to the image plane. The amplitude distribution $W(\vec{x})$ is zero everywhere outside the illuminated portion of the aperture.

Dividing the aperture into N identical elements of area $a = A/N$, Eq. (1a) becomes

$$U(\vec{q}) = \frac{1}{\lambda R}\sqrt{\frac{E}{A}} \iint_a e^{-i\vec{q}\cdot\vec{\xi}}\, d^2\xi \times \sum_{j=1}^{N} W(\vec{x}_j)\, e^{-i[\vec{q}\cdot\vec{x}_j + \phi(x_j)]} \ , \qquad (2)$$

where it is assumed that the amplitude weight and the intrinsic phase error of the beam vary slowly enough to be considered constant over each element. The vector $\vec{\xi}$ is the position within an element, relative

to $\vec{x}_j$, the position (e.g., centroid) of the j^{th} element. The intensity calculated from this expression is of the form

$$I(\vec{q}) = |U(\vec{q})|^2 = N I_0(\vec{q}) G(\vec{q}) , \tag{3a}$$

where

$$I_0(\vec{q}) = \frac{E}{\lambda^2 R^2 A} \left| \iint_a e^{-i\vec{q}\cdot\vec{\xi}} d^2\xi \right|^2 . \tag{3b}$$

The form is that of the diffraction-limited intensity distribution of the individual element, $I_0(\vec{q})$, modulated by the function

$$G(\vec{q}) = 1 + \sum_{\Delta\vec{x}\in S} e^{-i\vec{q}\cdot\Delta\vec{x}} C(\Delta\vec{x}), \tag{3c}$$

where

$$C(\Delta\vec{x}) = \frac{1}{N}\sum_{k=1}^{N} W(\vec{x}_k) W(\vec{x}_k + \Delta\vec{x})\, e^{i[\phi(\vec{x}_k) - \phi(\vec{x}_k + \Delta\vec{x})]} , \tag{3d}$$

which is of the form of a Fourier series with coefficients given by the correlation function $C(\Delta\vec{x})$ of the phase distribution $\phi(\vec{x})$. The summation in Eq. (3c) is taken over all vectors in the set $S \equiv \{\Delta\vec{x}_{jk}\}$, the set of all distinct inter-element displacement vectors, $\Delta\vec{x}_{jk} \equiv \vec{x}_j - \vec{x}_k$. From Eq. (3d), it is clear that reducing spatial correlations in the net phase distribution will reduce the modulation of the focused intensity distribution. Even though Eqs. (3a)–(3d) are general enough to include a nonuniform amplitude distribution in the incident beam, a uniform distribution will be assumed in all computed examples to follow. To a good degree of accuracy, this is consistent with what has been achieved.[6]

The form of the intensity distribution and the modulation function is clearer in the one-dimensional case. For a DPP of length L with N elements, the intensity distribution takes the form

$$I(p) = N I_0(p) G(p) , \tag{4a}$$

where the smooth profile

$$I_0(p) = \frac{EL}{\lambda RN} \frac{\sin^2\theta}{\theta^2} \tag{4b}$$

is modulated by the function

$$G(p) = 1 + \sum_{n=1}^{N-1} [g_n \cos 2n\theta + h_n \sin 2n\theta] , \tag{4c}$$

where the diffraction angle p is given by

$$p = \frac{\lambda N \theta}{\pi L} \quad . \tag{4d}$$

For the case of a plane wave incident on a DPP, the intrinsic phase error of the beam is zero, so $\phi(\vec{x}_j) = \phi_j$, the intrinsic phase alone, which is 0 or π, and one obtains $h_n = 0$ and

$$g_n = \frac{2}{N} \sum_{j=1}^{N-n} \cos\phi_j \cos\phi_{j+n} \quad , \tag{5}$$

If the phases of the DPP elements $\{\phi_j\}$ are chosen at random, then this quantity generally follows the root-N statistics of accumulated random steps,[8]

$$|g_n| \approx \frac{2\sqrt{N-n}}{N} \tag{6}$$

but smaller values can be obtained if the DPP element phases are chosen appropriately.

Construction of a reduced-correlation pattern proceeds by setting the phase of each element, one at a time, to the value that minimizes a predefined measure of correlation among all the previously defined elements. The construction begins from a small (e.g., 2 × 2) seed array. The correlation measure to be minimized is the square of the correlation function of all the defined elements, summed over the domain of correlation reduction, which can be any subset of $\{\Delta\vec{x}_{jk}\}$, the set of interelement displacements. One such measure is given by

$$Q(n_0) = \sum_{n=1}^{n_0} G_n^2 \quad , \tag{7a}$$

where

$$G_n^2 = \sum_{\Delta\vec{x} \in S_n} |C(\Delta\vec{x})|^2 \quad . \tag{7b}$$

The summation in this expression is taken over

$$S_n \quad \{\Delta\vec{x}_{jk} | n \geq |\Delta\vec{x}_{jk}| > n-1\} \quad ,$$

the subset of all distinct displacement vectors that fall within the specified range of length. Equation (7b) is evaluated only in terms of the defined pattern elements. The parameter n_0 defines the domain, or "range," of correlation reduction expressed in units of the period of the DPP pattern's underlying lattice. The quantity G_n is a direction average of the autocorrelation function over a unit range of separations. For this criterion, then, the domain of correlation

reduction is the set of all separations, up to n_0 "elements" or array spacings. In the case of the one-dimensional DPP, we have $G_n = g_n$, and this criterion reduces to that of minimizing the quantity

$$Q(n_0) = \sum_{n=1}^{n_0} |g_n|^2 \ . \tag{8}$$

If the choice of phase for an element is indeterminate, then the setting is made that tends to equalize the number of elements among the possible choices. The patterns we obtain are completely random in appearance, but they are not random because their correlation properties are not those of random patterns.

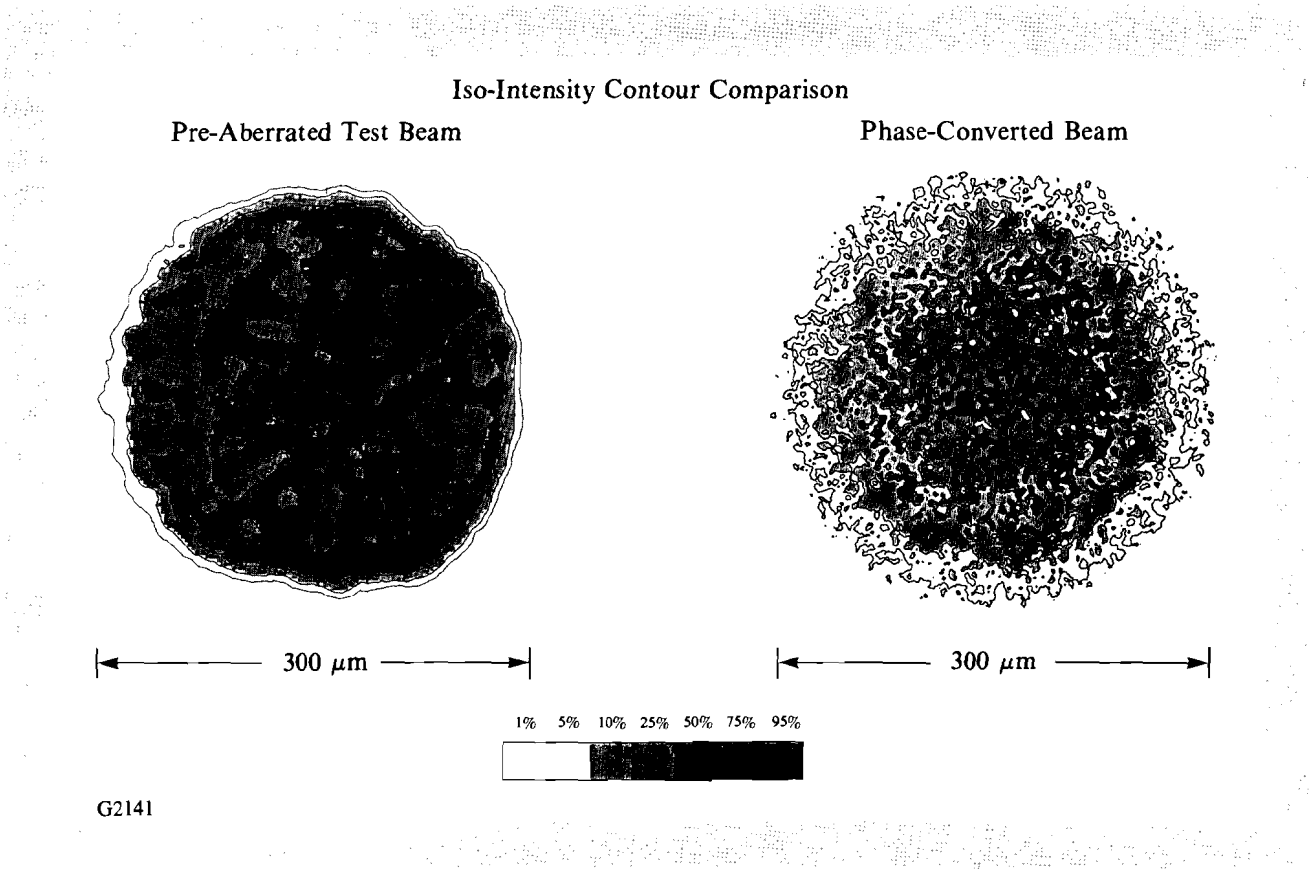

Fig. 40.10
The phase redistribution by a DPP converts a beam that can produce, at best, a coarsely modulated illumination pattern into a beam whose focused illumination pattern has the form of a high-intensity, short-scale structure superimposed upon a smooth diffraction-limited distribution of a single element.

This construction method is easily generalized to any regular array of a single equilateral or stretched shape that can completely tile a surface, such as, in the case of OMEGA,[3] hexagons. Also, more than two phase levels can be considered,[9] and any domain of correlation

reduction can be chosen. Modulations of any wavelength and orientation can be reduced, as long as the corresponding set of correlation displacements can be identified.

Elements need not be chosen in any particular order, other than that each new element should be contiguous to the previously set elements. This causes the choice of phase for the new element to be based on correlations with as many previously set elements as possible. At any stage in the construction, the set of defined elements should completely cover the area enclosed by a reasonably smooth, simple closed boundary. Since the correlations over the domain of correlation reduction are kept low throughout the construction of the pattern, as the area grows, the pattern has the desirable property that any piece of it also has reduced-correlation properties. Appropriate terminology for this property is "local nonredundancy" because the repetitiveness of the pattern found in any neighborhood in the pattern is less pronounced than the fortuitous repetition typical of a random pattern. Thus, one can expect improved uniformity, even if only a part of the DPP is illuminated or the illumination of the aperture is not perfectly uniform. In choosing possible DPP patterns, the preservation of reduced spatial correlations for a realistic variety of aperture illuminations can be an important consideration.

Lower autocorrelation values overall are obtained if the pattern is constructed only within the portion of the aperture to be illuminated because then the phase settings of the elements are not biased by their correlations with irrelevant, unilluminated elements. Iterating the pattern construction does give a slight additional reduction in correlations, but since all the phase elements have been set in the first iteration, the figure of merit becomes the sum over the entire pattern. Consequently, additional reduction in the figure of merit can come at the cost of degrading the local nonredundancy. The benefits and drawbacks of iteration and adjustments in the domain of the correlation reduction are best considered in the context of a specific application. If bench tests of reduced-correlation DPP's are sufficiently encouraging, further optimization will be undertaken.

To date, there has been no reported application of nonrandom patterns to DPP technology, so far as we are aware, but it has been anticipated for many years that arrays with controlled correlation properties would be useful in optical signal processing and pattern recognition.[10] For example, "pseudo-noise arrays"[11] have been developed[12,13] as the imaging elements in x-ray and gamma-ray optics.[14] Construction of arrays can proceed according to number-theoretical methods[10,11] as well as by choice, one element at a time, according to some criterion.[15] In this work, we have employed element-by-element construction because it offers much greater flexibility in array shape and size and, as was discussed above, a tolerance for variations in which a portion of the DPP is illuminated. The known pseudo-noise arrays are rectangular patterns of restricted dimensions. They must be formed into periodic mosaics, not only to form masks of a desired size and arrays of a desired total dimension, but also because their characteristic correlation functions are defined in

terms of cyclic sums that apply specifically to periodic arrays, rather than to a single array. Some pseudo-noise arrays are characterized by their correlations with special decoding arrays, rather than in terms of autocorrelations,[12,13] and these arrays obviously cannot be used in DPP's. Progress in relaxing dimension restrictions has been made,[13] but the resulting arrays contain many more elements of one value than the other, which leads to undesirable coherent-interference effects in the irradiation distribution. In spite of these difficulties, the possibility that the existing theory of pseudo-noise arrays might lead to arrays that are advantageous as DPP patterns deserves attention.

Examples of intensity distributions shown in this article are obtained by numerically evaluating Eqs. (1) and (3) in terms of net phase distributions.[16] In all cases, square DPP grids of various dimensions are assumed, and it will be made clear in each example whether the net phase includes the DPP contribution alone, or whether an assumed intrinsic phase error is included. In Fig. 40.11, the first example shows, by comparison, the effect of reducing correlations up to separations of 30 times the grid spacing in a DPP of dimension 75×75. The aperture is the inscribed circular area of the square array. The intensity profile along one axis of the intensity distribution is shown. The smooth curve in each frame is the ideal unmodulated profile given by Eqs. (3a) and (3b) for the case $G(\vec{q}) = 1$. To allow the long-wavelength modulations to be seen more clearly, a numerical smoothing over about 1% of the profile width has been applied in the corresponding lower frames. With short-range correlations in the DPP reduced, the long-scale modulations of the profile are noticeably smaller.

The quantity G_n given by Eq. (7b) is a useful measure of the autocorrelation spectrum that can be plotted as a function of n to show the distribution of modulation amplitude as a function of spatial frequency. Roughly speaking, G_n includes spatial frequencies from $2(n - 1)$ to $2n$ modulation periods within the central lobe of the profile width. Comparing plots of G_n versus n usually gives a better visualization of modulation reduction than comparisons of irradiation profiles.

In Fig. 40.12, G_n is plotted for the phase distributions of three different square (40×40) reduced-correlation DPP's and a random DPP. The reductions in autocorrelation relative to the random DPP are clearly seen for each of the three different ranges. Here, as in every other instance considered, with or without background phase error, correlations do not increase for separations over which correlations were not reduced. This is very important not only because it makes improved uniformity possible, but it is also not necessarily the expected result. Since the choice of a single-element phase affects the autocorrelation function for all separations up to the furthest-removed boundary element, reducing correlations over one range of separations affects correlations at other separations; we are aware of no reason why correlations over displacements not included in the choice criterion are not enhanced. Fortunately, correlation reduction does not appear to introduce correlations at any separation that are stronger than

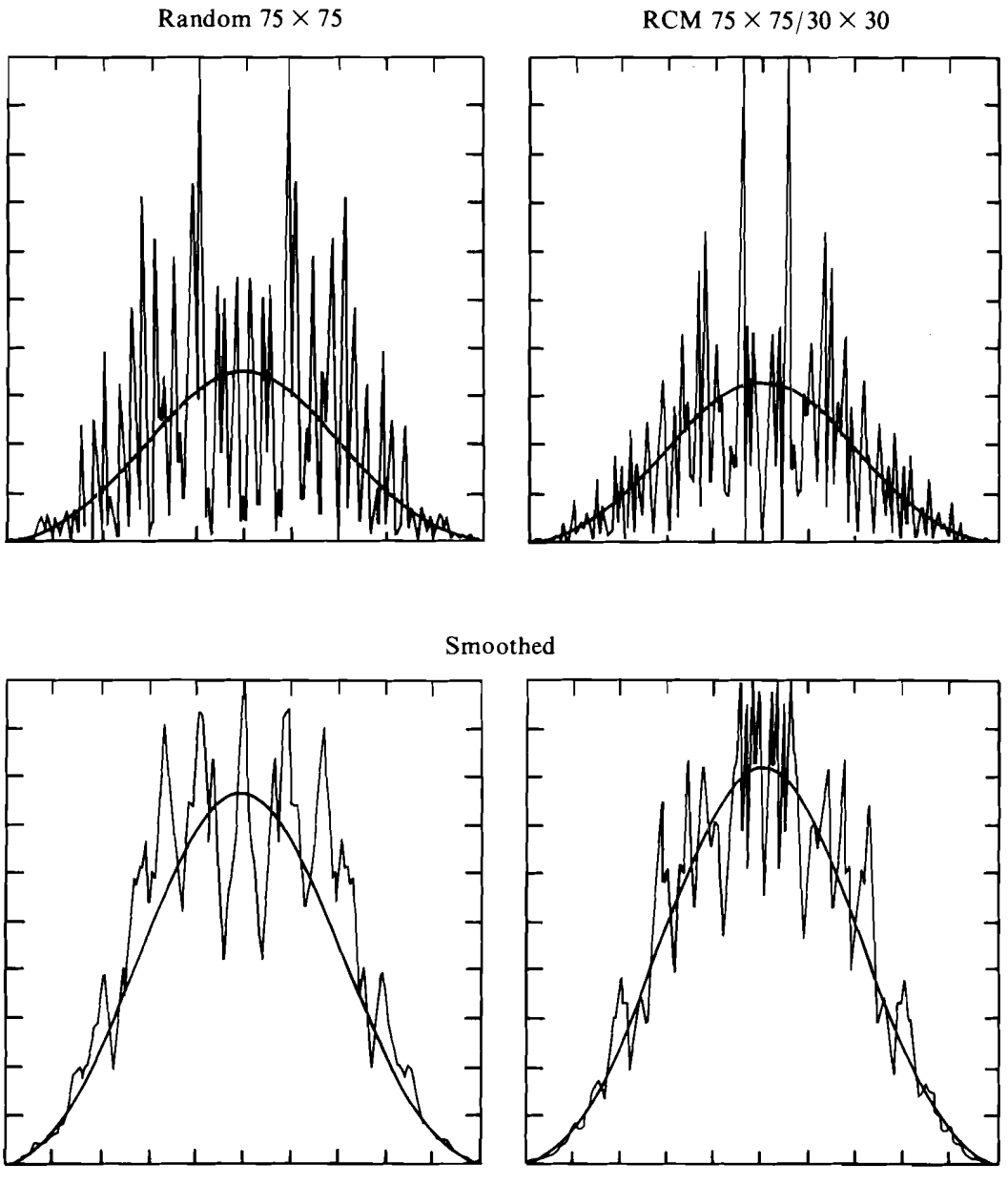

Fig. 40.11
A pair of profiles of simulated intensity distributions given by 75 × 75 DPP's illustrates the effect of reducing correlations at separations of up to 30 elements. The ideal unmodulated intensity profile is superimposed for comparison. By reducing longer-wavelength modulations, correlation reduction causes the modulation to follow the ideal profile more closely. The two profiles are repeated below with a smoothing over about 1% of the profile width to allow easier comparison of the longer-wavelength modulations.

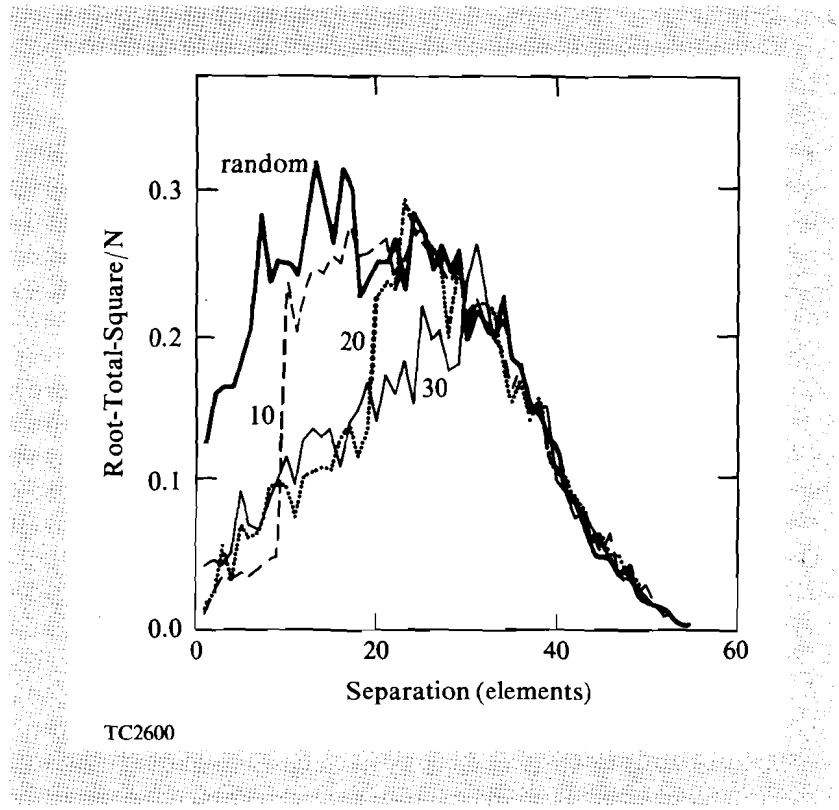

Fig. 40.12
The autocorrelation spectrum is plotted for 4 different 40 × 40 patterns. Lower correlations are obtained up to the correlation-reduction range and correlations outside this range are not increased above the level for a random pattern.

those that typically occur in random DPP's, which suggests that reduced-correlation DPP's can always be expected to perform better than random ones.

Correlation reduction in partially illuminated DPP's is demonstrated in Fig. 40.13 by comparing the autocorrelation spectra of five DPP's, each of dimension 20 × 20 and filling the same square aperture. The four patterns represented by curves (a)–(d) were all constructed with a correlation-reduction range of 10. Curve (a) represents a DPP array constructed only within the aperture. Curves (b)–(d) represent DPP's that are the center 20 × 20 sections of larger arrays of dimension 30 × 30, 40 × 40, and 50 × 50, respectively. All are to be compared with the random DPP represented by curve (e). Sizeable fluctuations in the correlations are caused by the relatively small number of elements in the illuminated pattern. The curve for the random case is an average spectrum derived statistically from the square root of the number of element pairs that fall within each separation bin. Consequently, it appears smoother than the other curves. Curves (a)-(d) all show correlations reduced below random levels, and, as was explained above, the correlation reduction is distinctly better in the pattern constructed only within the aperture.

An important question to consider is the degree of improvement obtained when the net phase distribution of the beam emerging from the DPP includes a typical level of phase error from the beam itself. The intrinsic phase distribution of the beam in the aperture plane is the critical limitation on the improvement in uniformity that can be

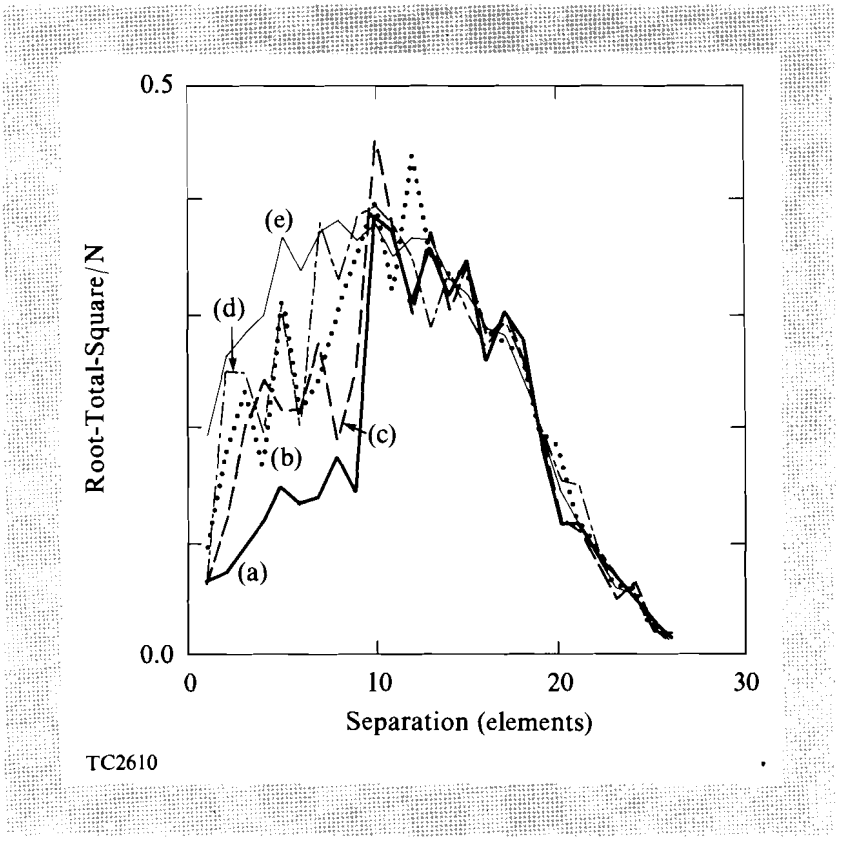

Fig. 40.13
Autocorrelation sums for five different DPP's are plotted. The range of correlation reduction in each case is 10, and the illuminated area is the entire 20 × 20 array. Curve (a) is derived from the pattern constructed only within the illuminated area. Curves (b)–(d) represent illuminated areas that are the center portions of larger patterns (30 × 30, 40 × 40, and 50 × 50, respectively), and curve (e) is the crude statistical result for a random pattern. While the greatest reduction of correlations occurs when the pattern is constructed only within the illuminated area, reduction is also obtained when only a small part of the aperture is illuminated.

obtained using reduced-correlation DPP's. For the purposes of this discussion, we will take the measured phase distribution of one beam of the OMEGA laser as typical.[6] This beam was chosen in advance of the phase measurement for its relatively good near-field amplitude uniformity, which is not necessarily a predictor of good phase uniformity. Profiles of this phase distribution along two orthogonal axes are plotted in Fig. 40.14. The effect of this typical intrinsic phase on focused intensity distributions is shown by the examples in Fig. 40.15. In these simulations, DPP's of dimension 75 × 75 were assumed, and a correlation-reduction range of ten grid spacings was used in the correlation-reduction case. Profiles along two orthogonal axes are shown. As in the bottom frames of Fig. 40.11, the profiles here are smoothed over about 1% of the beam radius. Even with the typical phase error in the beam, the focused-intensity profiles are noticeably improved with a reduced-correlation DPP.

As the intrinsic phase error of a beam is increased, the spatial-autocorrelation spectrum of net phase distribution begins to lose the nonrandom character of the DPP phase distribution. This is illustrated in Fig. 40.16 using a DPP pattern of dimension 100 × 100 and a correlation-reduction range of 30. At distances over which the intrinsic phase error varies by about a quarter wave, the half-wave contribution of the DPP to the net phase is obscured. At shorter separations where the phase error changes by a small fraction of a wave, the nonrandom correlation is left largely intact. Consequently, as the phase error is increased, degradation of the correlation reduction occurs first at the

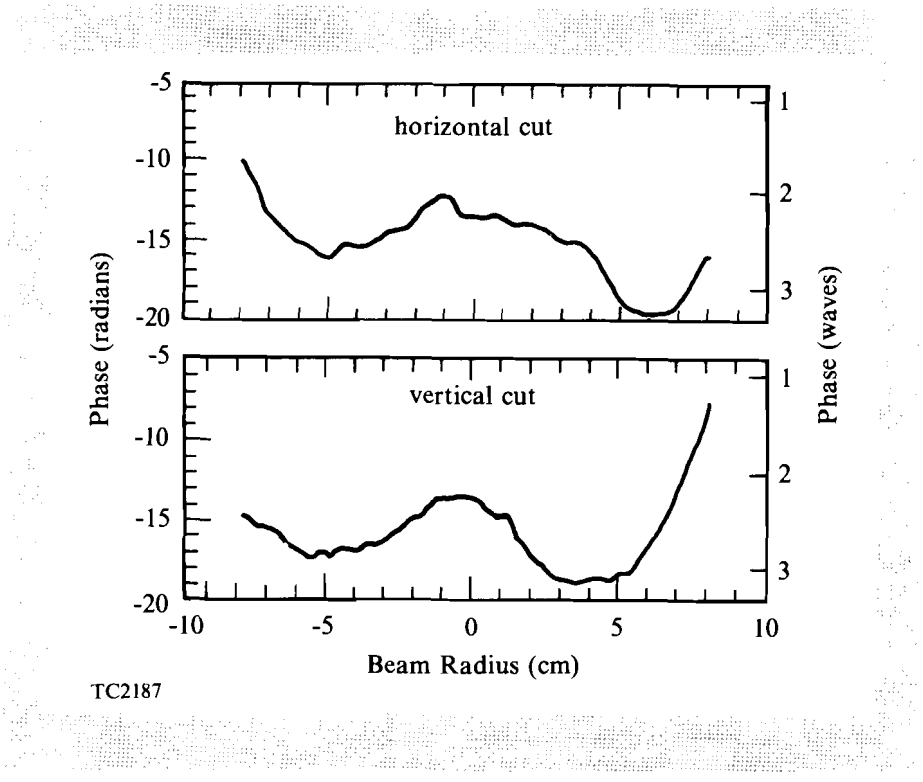

Fig. 40.14
The measured intrinsic phase error for a typical OMEGA beam is plotted along two axes of the aperture plane.

longer separations. Correlation reduction at the shortest separations, those corresponding to the long-scale illumination nonuniformities, is least affected by the phase error of the beam. As a result, substantial improvement at these longer wavelengths is still obtained with the full level of typical phase error. This gives hope that improvement in long-wavelength uniformity might be possible in future experiments. Figure 40.17 includes a magnified detail of the short-range autocorrelation of the net phase. Again, it is important to note that the contribution of the intrinsic phase error does not increase the correlations of the net phase above random levels.

The performance of ICF targets depends on the magnitude and spatial-wavelength content of the irradiation nonuniformity on a spherical surface.[17] The nonuniformity of the spherical irradiation has been calculated for the 24-beam distribution used on the OMEGA laser system in terms of a single-beam irradiance distribution, plus a random rotation, at the appropriate positions on a sphere representing the target surface. The resulting spherical-illumination pattern is decomposed into spherical harmonics to examine the spatial-wavelength content of the nonuniformity on target.[16] Two spherical-mode decompositions of the illumination nonuniformity obtained using reduced-correlation DPP's, with and without the typical phase error, are shown as bar graphs of the modal amplitude in Fig. 40.18. DPP's of 75 × 75 elements with a correlation-reduction range of 30 grid

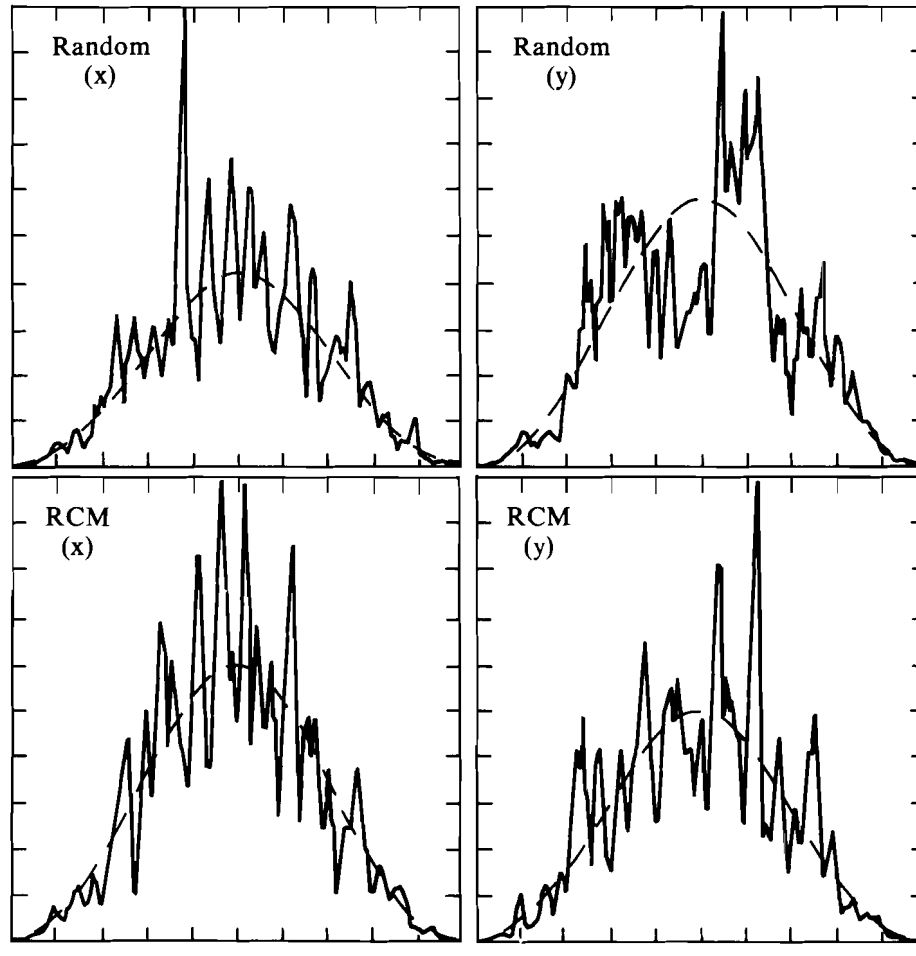

Fig. 40.15
Orthogonal profiles of a simulated intensity distribution for 75 × 75 DPP's, including the effect of the "typical" phase error shown in Fig. 40.14. Correlations have been reduced up to a range of 10. A lower level of modulation, particularly at longer wavelengths, is seen using the reduced-correlation DPP's.

spacings were assumed. The improvement resulting from correlation reduction is seen by comparing the bar height with the solid curve, which represents an average of three simulations done with random DPP's. Improvement is obtained throughout the mode spectrum for the case of no phase error, while significant and repeatable improvement is seen only for modes up to $\ell \approx 7$ for the case including phase error. The deviation of the "random" curve from the amplitudes of higher modes, say $\ell \gtrsim 20$, is indicative of the level of chance variations due to the use of differently seeded DPP's, different orientations of the beams, and different relative orientations of the DPP phase profile and the intrinsic phase distribution of the beam, all of which were varied in

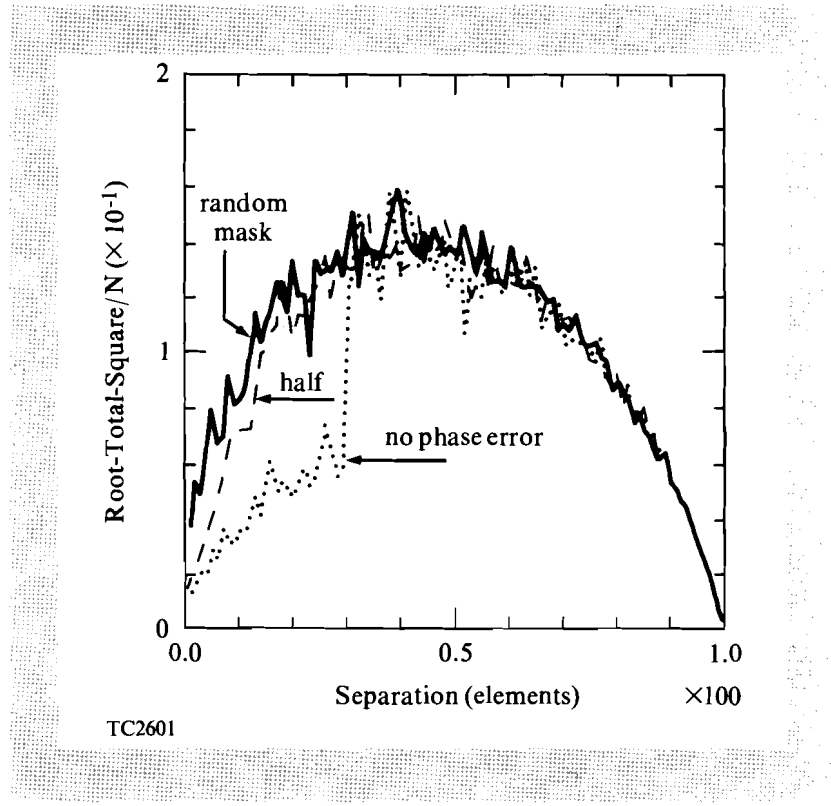

Fig. 40.16
The effect of phase error is seen in this comparison of autocorrelation functions of the net phase with a 100 × 100 DPP for various multiples of the "typical" phase-error distribution. Correlations in the DPP are reduced up to a range of 30 elements. As the phase error increases, correlations are randomized for all but the shortest separations.

the simulations. The solid segments in the bar graphs are the mode amplitudes that would be obtained for perfect, unmodulated beams.

To more clearly see the potential decrease in long-scale nonuniformity by applying reduced-correlation DPP's to a 24-beam system, the root-total-square nonuniformity of the first five modes is plotted in Fig. 40.19 in histograms of the simulations done to date. Again, DPP's of dimension 75 × 75 and correlation-reduction range 30 were assumed. To facilitate comparison, separate histograms are shown for perfect beams $[G(\vec{q})=1]$, for reduced-correlation DPP's, and for random DPP's. Differences among simulations of the same type are explained above. The range of improvement using correlation reduction is comparable to the effect of a random 4%-rms beam-to-beam energy imbalance that was introduced into a few of the simulations indicated in order to allow comparison of correlation effects with a relatively well-understood source of illumination nonuniformity. The histograms suggest a possible distribution of outcomes, which gives a sense of how "lucky" or "unlucky" one might be with a given DPP and beam. In practice, the distribution will be somewhat narrower because the intrinsic phase distribution will vary from beam to beam, which will allow the natural random variability of results to average out more than in the simulations where the net phase profiles vary only by a random rotation. On the OMEGA system, the aperture, focal length, and target size require DPP arrays roughly a factor of 2 larger than the 75 × 75 square arrays assumed in the simulation, and the results could differ slightly. With an array of larger dimensions, a given modulation mode [e.g., a single term in

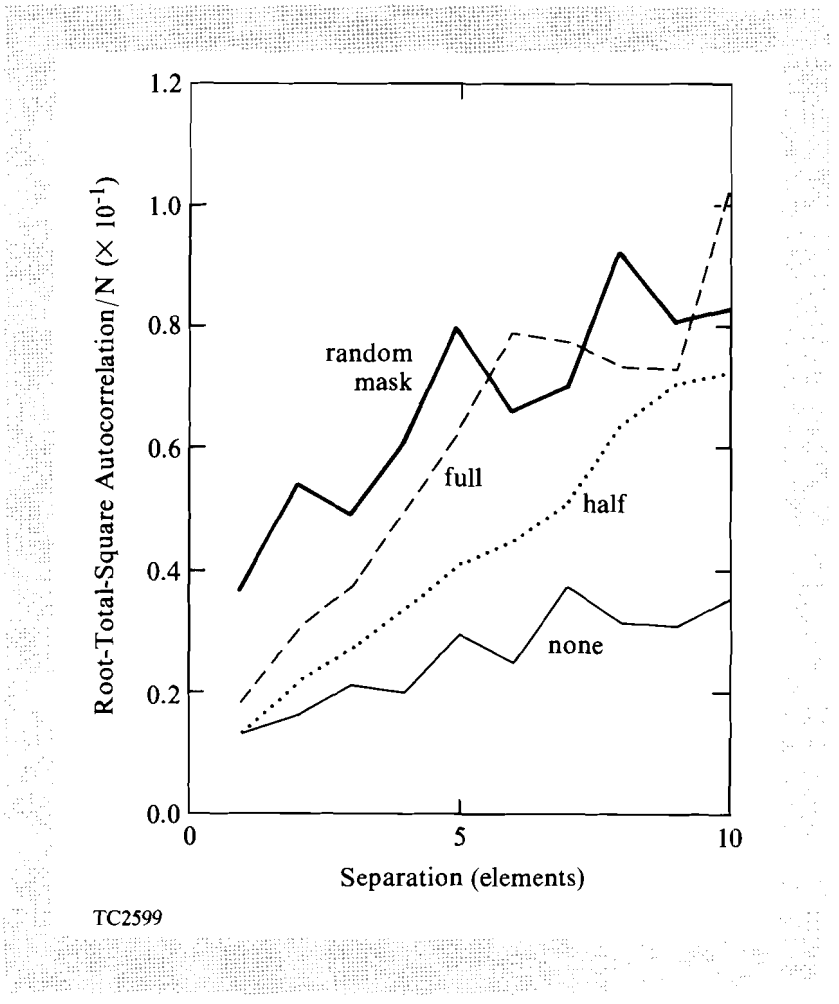

Fig. 40.17
This figure is a magnified detail of Fig. 40.16 showing that correlations in the net phase are effectively randomized by the phase error of the beam, except at the very shortest separations, over which differences in phase error are only a small fraction of a wave.

Eq. (3c) or a given n term in Eq. (4c)] is produced by element pairs closer to each other, which results in smaller differences in intrinsic beam phase between element pairs and thus less disruption of the reduced phase correlations. On the other hand, the relative amplitude of this modulation mode would be reduced by the large-number statistics of the increased number of identically displaced element pairs.

Correlation reduction represents a potentially useful complement to SSD. Even though correlation reduction would have a relatively small impact on the total nonuniformity spectrum, compared with the major degree of improvement from SSD,[5] additional reduction in nonuniformity would occur in the lowest-order modes of nonuniformity where SSD is least effective. In SSD, the reduction of nonuniformity results from averaging away the interference effects with time-varying color differences among different DPP elements. Since these color differences are smallest over the shortest separations, SSD requires the longest averaging times for smoothing the longest-scale nonuniformity. The reduction of phase correlations over these small separations would reduce long-scale nonuniformity instantaneously. Given the stringent uniformity requirements and

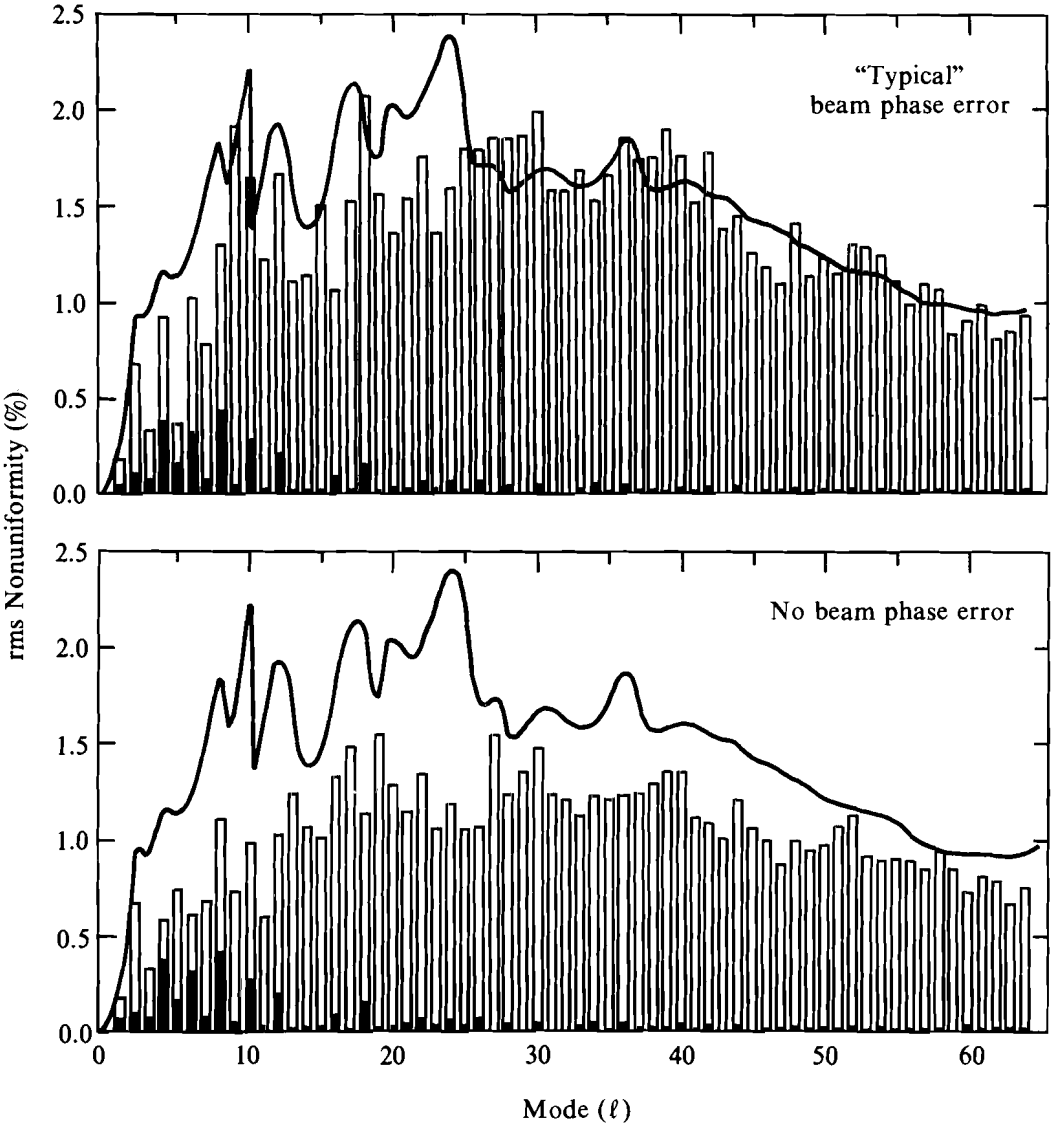

Fig. 40.18
To show the improvement in a simulated 24-beam illumination pattern resulting from correlation reduction, the spectrum of spherical-harmonic modes of the illumination can be compared to the solid curve, which represents an average of three simulations done with random DPP's. DPP's of 75 × 75 elements were used with a correlation-reduction range of 30 elements, and cases both with and without phase error are shown. Improvement is obtained throughout the spectrum for the case of no phase error, while significant improvement is seen only for modes up to about $\ell = 7$ for the case including phase error. The degree of deviation of the "random" curve from the mode amplitudes in the upper bar graph for the higher modes, say $\ell > 20$, is not significant. Solid bars show the mode amplitudes obtained using perfect, unmodulated beams.

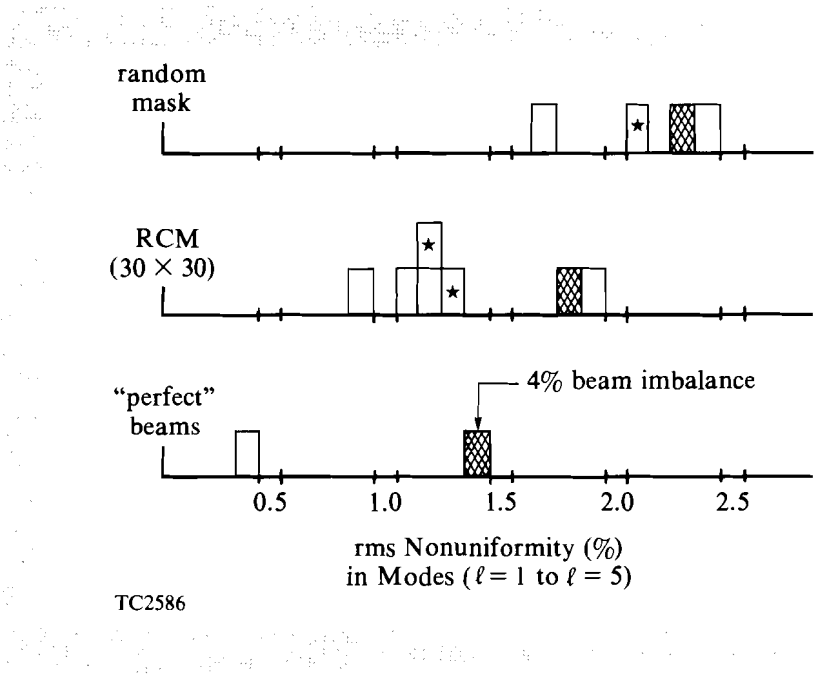

Fig. 40.19
The consistency of improvement in the lowest modes of the simulated uniformity using reduced-correlation DPP's is seen in this set of histograms. Each rectangle represents one simulation. Simulations differ in their arbitrary initializations, the neglect of phase error (indicated by a star), or the addition of a 4% beam imbalance (shading). The simulations assume 24-beam illumination using 75 × 75 DPP's and a correlation-reduction range of 30 elements. Correlation reduction typically reduces these modes significantly closer to the level expected for perfect, unmodulated beams.

averaging-time limitations of high-compression experiments,[17] even a modest improvement of this kind could be crucial.

Reduced-correlation DPP's could be useful in holography, the original intended application of DPP's.[1] The design of lasers with low phase error would not be as constrained by the need for high power as in ICF, and more control over illumination uniformity could be exercised.

The possibility that random patterns are not optimum for DPP's is an intriguing question of principle. For improving the illumination uniformity of a focused laser beam, it is now clear that more effective patterns exist and that reduced-correlation patterns might lead to useful reductions in long-wavelength illumination nonuniformities. The degree of improvement in the spherical-illumination uniformity can range from nil to a factor-of-2 reduction in low-order modes, depending on the intrinsic phase error of the beam. For a typical level of phase error in a high-quality, high-intensity laser, such a degree of improvement might be possible. Reduced-correlation DPP's will cost no more to implement than random DPP's, and from all indications, they are virtually risk-free. At worst, they are effectively equivalent to a random mask when overwhelmed by phase error in the beam. Experiments now in progress will better determine the utility of these new patterns.

ACKNOWLEDGMENT

This work was supported by the U.S. Department of Energy Office of Inertial Fusion under agreement No. DE-FC03-85DP40200 and by the Laser Fusion Feasibility Project at the Laboratory for Laser Energetics, which has the following sponsors: Empire State Electric Energy Research Corporation, New York State Energy Research and Development Authority, Ontario Hydro, and the University of Rochester. Such support does not imply endorsement of the content by any of the above parties.

REFERENCES

1. C. B. Burckhardt, *Appl. Opt.* **9**, 695 (1970).
2. Y. Kato and K. Mima, *Appl. Phys. B* **29**, 186 (1982); Y. Kato *et al., Phys. Rev. Lett.* **53**, 1057 (1984).
3. LLE Review **33**, 1 (1987).
4. M. Born and E. Wolf, *Principles of Optics,* 6th corrected edition, (Pergamon Press, New York, 1980).
5. S. Skupsky, R. W. Short, T. Kessler, R. S. Craxton, S. Letzring, and J. M. Soures, to be published in *J. Appl. Phys.* See also: LLE Review **36**, 158 (1988); LLE Review **37**, 29 (1988); **37**, 40 (1988).
6. S. Skupsky and T. Kessler, *Opt. Commun.* **70**, 123 (1989). See also: LLE Review **31**, 106 (1987).
7. R. H. Lehmberg and S. P. Obenschain, *Opt. Commun.* **46**, 27 (1983).
8. Y. Takeda, Y. Oshida, and Y. Miyamura, *Appl. Opt.* **11**, 818 (1972).
9. F. J. MacWilliams and N. J. A. Sloane, *Proc. of IEEE* **64**, 1715 (1976), and references therein.
10. D. Calabro and J. K. Wolf, *Inform. and Control* **11**, 537 (1967).
11. T. M. Cannon and E. E. Fenimore, *IEEE Trans. Nucl. Sci.* **NS-25**, 184 (1978).
12. A. R. Gourlay and J. B. Stephen, *Appl. Opt.* **22**, 4042 (1983); S. R. Gottesman and E. J. Schneid, *IEEE Trans. Nucl. Sci.* **33**, 745 (1986).
13. E. E. Fenimore and T. M. Cannon, *Appl. Opt.* **17**, 337 (1978).
14. M. J. E. Golay, *J. Opt. Soc. Am.* **61**, 272 (1971).
15. W. C. Stewart, A. H. Firester, and E. C. Fox, *Appl. Opt.* **11**, 604 (1972).
16. S. Skupsky and K. Lee, *J. Appl. Phys.* **54**, 3662 (1987).
17. LLE Review **37**, 2 (1988).

2.B Uniform Liquid-Fuel Layer Produced in a Cryogenic Target by a Time-Dependent Thermal Gradient

In inertial fusion experiments, it is possible to achieve a higher-density compression by starting with the DT fuel in a condensed state instead of a gaseous state at room temperature. Because of the uniformity requirements of direct-drive inertial fusion, the DT condensate must be in the form of a highly uniform and spherically symmetric layer on the interior surface of the cryogenically cooled fuel capsule. Prior efforts to fabricate such a target have included instant refreeze of the fuel after vaporization with a laser pulse,[1,2] absorption of the fuel in a foam layer,[3–5] redistribution of the fuel by beta-decay heating,[6,7] and the application of a static thermal gradient to overcome gravity-induced sag of liquid fuel.[8–13] A unique set of difficulties is encountered in deploying each of these techniques in the target chamber of a multibeam laser. In this study, a time-dependent thermal gradient is applied to a target that has been cooled by helium gas jets. The liquid-DT fuel, initially thicker at the bottom of the shell, is redistributed, and a momentary state of uniformity is observed. Continuing its motion, the fuel subsequently becomes thicker at the top of the shell. Suitable timing of the applied thermal gradient can provide fuel-layer uniformity at the moment the drive laser is fired. This method works in the presence of room-temperature thermal radiation, while not obstructing any of the beams of the drive laser. The necessity for a retractable isothermal shroud (used in instant refreeze and other techniques) is thus eliminated. In addition, this method works for thicker condensed-DT layers than can be made uniform with the instant-refreeze technique.

Several studies[8–13] have described how DT or D_2 liquid should become uniformly distributed on the wall of a shell when a suitable static thermal gradient is applied to overcome gravity-induced nonuniformity. The phenomenon is explained as a balance among gravity, surface tension, and a dynamic equilibrium of evaporation, recondensation, and liquid flow. In the case of DT, a multicomponent fluid (D_2, T_2, and DT), some fractionation occurs, with the warmest spots developing the highest concentrations of T_2, the least volatile component. A prediction of this model, that with D_2 (a single-component fluid) uniformity is achieved by making the top of the target colder than the bottom, whereas with DT, the reverse is true, was demonstrated experimentally by Kim and Krahn.[8] Fuel uniformity was observed in only a single view, however, leaving open the possibility that, had the target been viewed from another direction, a nonuniform fuel distribution might have been seen. As in the Kim and Krahn study, the work described here employs opposing helium gas jets to cool the target and a three-axis translator to position the target between the nozzles. Important differences in this study include the use

of two-view interferometry, ohmic heating of the nozzles to apply the thermal gradient, a greater solid angle for incident room-temperature thermal radiation, a lower background pressure, and the finding that a time-dependent thermal gradient is required to achieve fuel uniformity.

The nozzle assembly, shown in Fig. 40.20, meets the requirements of (1) being able to cool a target to the freezing point of DT, (2) providing a vertical thermal gradient sufficient to produce liquid-DT-layer uniformity just above the freezing point, (3) being geometrically arranged so as not to obstruct any of the 24 beams of the OMEGA laser, and (4) being easily replaceable. This assembly is attached to a copper rod cooled by a liquid-helium cryostat. The base block, made of tellurium-copper, provides good thermal contact between the copper rod and the high-purity (99.99%) copper tubes leading to the nozzles. Lower-purity copper tubing was tried, but it lacked sufficient thermal conductivity. The nozzles are cylinders of electroformed copper, though short pieces of stainless steel tubing were also found to work. The inside diameter of the nozzles, $\sim 100\ \mu m$, is not critical: a nozzle

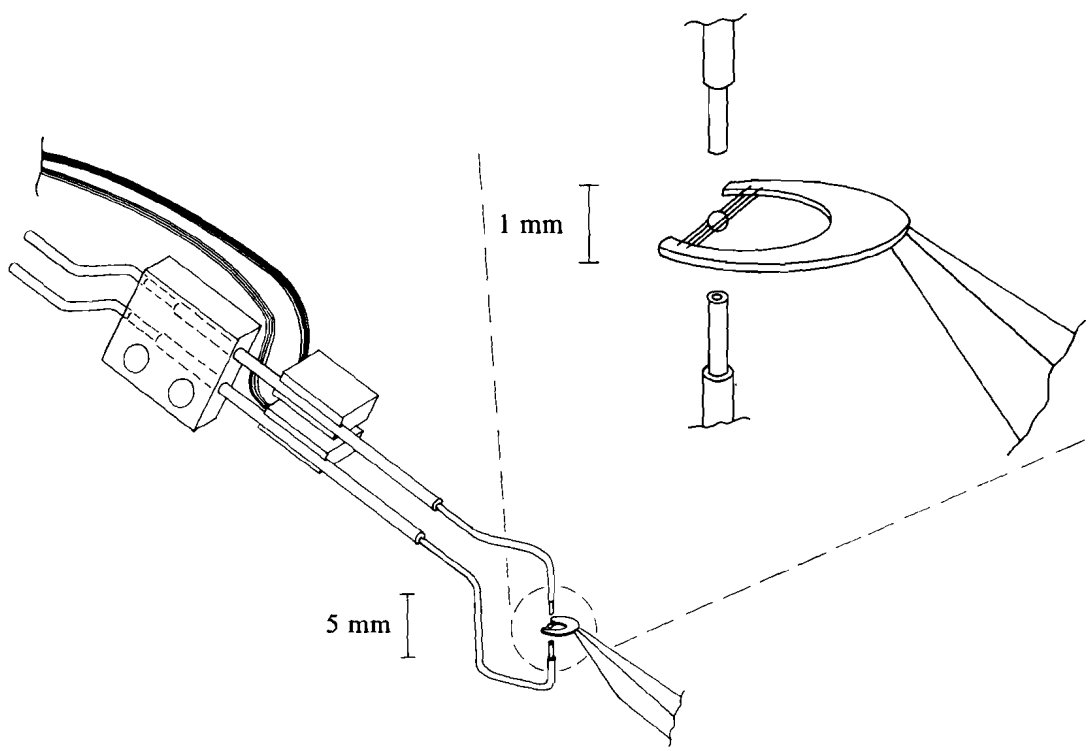

Fig. 40.20
Nozzle assembly with target and its support. When installed, the nozzles are vertical, and the target is positioned independently between the nozzles. The parts are precisely arranged so as not to obstruct the 24 beams of the OMEGA laser. Tubing parts are bent on precise fixtures and then clamped together on another fixture for soldering. The heater-thermometer assemblies are soldered on last.

diameter of 400 μm was also found to work for a 250-μm-diameter target. The main constraint on nozzle diameter is that the outer edge not obstruct beams of the OMEGA laser. Larger-diameter nozzles must be placed farther from the target, reducing cooling efficiency and requiring a greater flow of helium gas. The helium gas-supply tubes are stainless steel, bent to fit into a quickly demountable fixture sealed with compressed indium. Attached to each of the copper tubes is a heater-thermometer assembly with a silicon-diode thermometer and a heater consisting of coiled resistance wire. The thermometers are for diagnostic purposes and could be omitted in the future, since observations of freezing of the fuel provide adequate temperature data.

Preparing for application of the time-dependent thermal gradient entails setting up suitable ambient conditions of target position, helium gas flow, and nozzle temperature. After centering the target reasonably well (to ~ 50 μm) between the nozzles, gas flow is established using a pair of flow controllers. The initial flows of 30 to 60 μg/s to each nozzle can later be reduced. Heat exchangers cool the He gas to the temperature of the copper support rod (5°K in the absence of applied heat) before it enters the nozzle supply tubes. This flow of gas freezes the DT in the target. Sufficient heat is then supplied to the copper support rod to barely melt the DT, using a temperature controller. Next a series of small adjustments is made, in target position, temperature of the copper support rod, and finally differential heat to the nozzles, with the goal of getting the fuel as close as possible to a uniform state while just above the freezing point. Fuel uniformity is easily assessed at this stage by observing the interferometric video images of both views of the target with the interferometer set up for a constant-phase background. At this point it is possible to obtain uniformity in one view or the other, but with the alternative view showing a high degree of nonuniformity.

After these initial adjustments of the ambient conditions, a time-dependent thermal gradient is imposed using a repetitive cycle of several-seconds duration. In this cycle, the current applied to the upper nozzle heater is given a step increase, lasting 0.5 s or more, or the lower nozzle heater is given a step decrease, or both. As this cycle continues, further small adjustments are made in all the aforementioned quantities until the degree of momentary fuel uniformity is satisfactory, and one is assured that the fuel, when in the uniform state, is as close to the freezing point as possible, and gas flow is minimized. The final positioning adjustments of the target with respect to the nozzles are in 2- to 5-μm steps. The position must be adjusted to this precision in both lateral directions. As fuel uniformity is now a transient state, a video recorder is employed to help assess the uniformity and repeatability of this state.

Observation of fuel-layer uniformity requires a high degree of uniformity of the outer shell. This is assured by the shell-selection process prior to permeation of the shell with fuel. The shell is preselected[14] for wall thickness, and then rotated about two axes in a Mach-Zehnder interferometer so that uniformity is observed from three orthogonal directions. After permeation the shell is mounted, usually

between four submicron spider webs,[15] uniformly coated with 0.1 μm of parylene, and recharacterized in the cryogenic apparatus. For each step in the characterization process, interferograms are obtained from two directions at right angles to each other. A pair of shearing interferometers of new design is employed.[16] To assess uniformity, a constant-phase background is used, producing interference fringes that are circular and concentric if the target is uniform. If reasonable uniformity is found, a tilt is introduced in an interferometer mirror, producing a background fringe pattern of parallel lines. This "tilted-phase" interferogram allows greater accuracy in determining such parameters as wall thickness, fuel-gas density, or fraction of fuel condensed.

Complete characterization of a target is a three-step process. At each step, constant-phase and tilted-phase interferograms are taken from both directions. The first step is to use sufficiently cold gas flow from the nozzles to freeze all the fuel on the top or bottom of the target, allowing redetermination of the wall thickness and uniformity of the shell portion that is free of fuel. Next, the target is warmed, and interferograms of the gaseous state are taken to determine the fuel density, and therefore the total fuel content. Finally, interferograms of the uniform condensed state are taken, from which fuel uniformity and fraction condensed are determined. These three steps are illustrated in Fig. 40.21.

To assess the fuel content and distribution in a target, interferograms are matched with templates generated using a ray-tracing computation. For this computation the input parameters specific to the target are shell diameter, wall thickness, shell refractive index, fuel density in the gaseous state, fraction condensed, and fuel refractive index.[17,18] Templates can also be generated for low-order modes of fuel nonuniformity, especially decentration of a specified magnitude and direction. The parameters specific to the interferometer are wavelength, wave-front tilt (i.e., number of background fringes per unit length along each of the two axes of the interferogram), additive phase, magnification, and the focal ratio (f-number) of the collecting lens. The focal ratio determines the extent of a dark ring inside the edge of the target corresponding to rays refracted by the target beyond the edge of the collecting lens. The template generated is an array of 240 $\times$ 256 pixels showing points of constant phase on the wave front and the edge of the target. To test a match between a template and an image, the image (480 $\times$ 512 pixels, each with 256 levels) may be live or recorded on disk memory. The template, in color, is superimposed over the black-and-white image using a video monitor.

The central portion of each interferogram yields the optical path through the center of the target with a nonuniqueness of an integer number of waves. For example, if the observed fringe at the center of the target is dark and the central background fringe is light, the optical path through the center of the target is (m + 1/2) waves, where m is an unknown integer. In practice, comparison with the template over the whole field of view is usually sufficient to eliminate the nonuniqueness. First, an apparently acceptable match of a template to

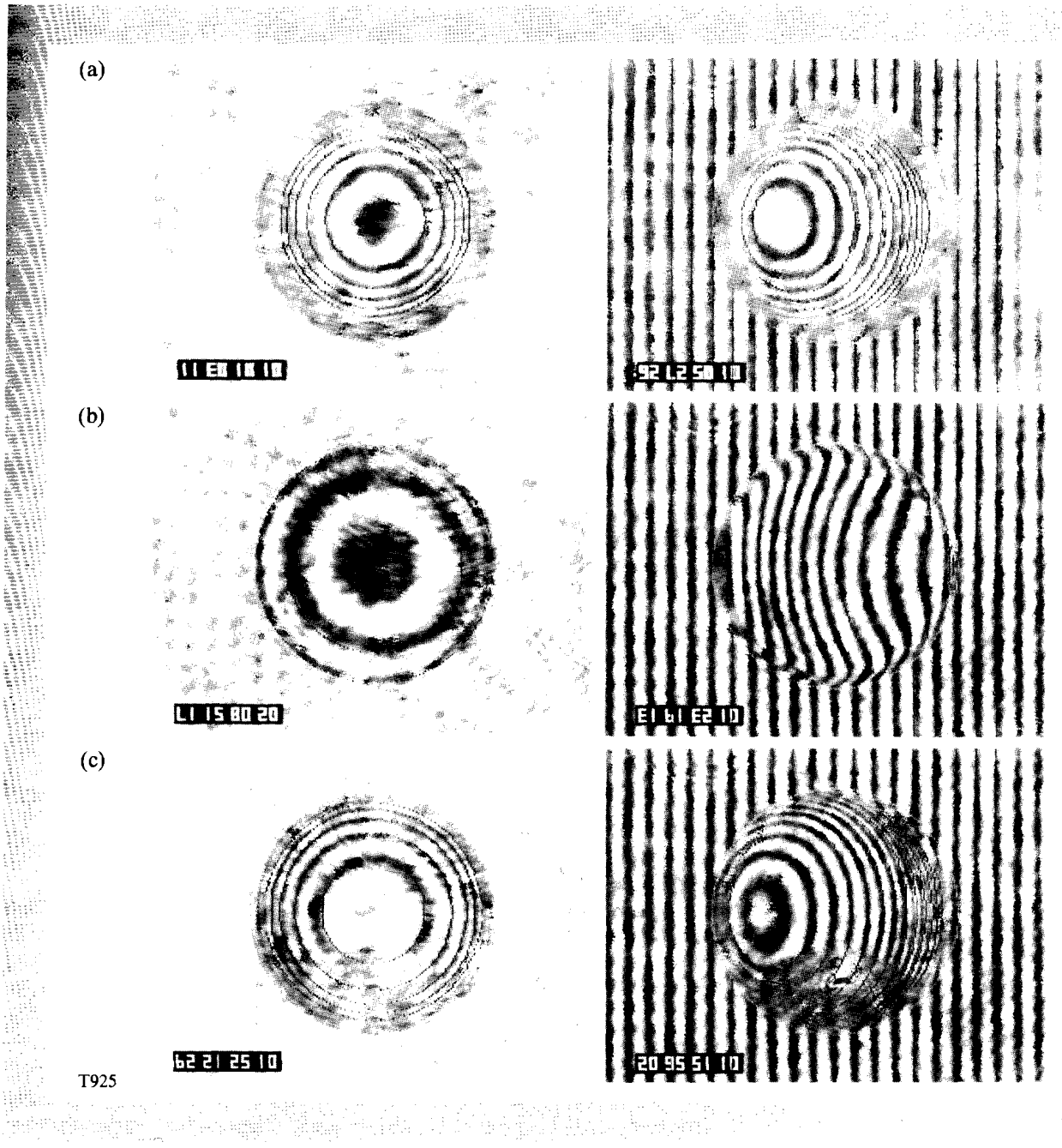

Fig. 40.21
Interferograms and templates (from one of the two views) needed to fully characterize a target. The constant-phase interferograms on the right demonstrate uniformity, while the tilted-phase interferograms on the left are used to measure target parameters by matching the templates to them. (a) Fuel is all frozen on top. Template match indicates the wall thickness* is 4.62 ± 0.1 μm. (b) Fuel is in the gaseous state. The pressure** of DT is found to be 171 ± 3 atm. (c) Fuel is momentarily in a uniform liquid layer with ~98% condensed. The other view also shows uniformity. The match of the templates to the interferograms is remarkably good in every detail. The templates may be recognized as thin uniform lines.
*This assumes precise knowledge of the index of refraction of the shell material.
**By "pressure" we mean here the pressure that would exist if DT obeyed the ideal gas law. In reality, this is a measurement of gas density.

an image is found with the fringes matching both outside and at the center of the target. Then the parameter being determined is increased or decreased by enough to shift the template by one fringe at the center of the target. The template will still be a good match near the center of the target. In most cases, however, the changed parameter can be accepted or rejected based on whether the match away from the center has improved or worsened. If one is still not certain of the uniqueness of the match, this can be resolved by changing the illumination wavelength and going through the matching process again. This technique enables the target parameter to be characterized to a high degree of accuracy, with errors corresponding to optical path changes approaching one tenth of the illumination wavelength.

By observing the freezing of the fuel at a variety of gas flows and nozzle temperatures, a useful equation can be obtained for target temperature as a function of these parameters. Since the target is exposed to room-temperature thermal radiation from nearly all directions, it absorbs power, $4\pi r^2 \sigma T_r^4 \epsilon$, where T_r is the (absolute) room temperature, r is the target radius, σ is the Stefan-Boltzmann constant, and ϵ is the emissivity of the target. This power is removed by the cooling power of the helium gas stream, $feC(T_n - T_t)$, where f is the total gas flow (mass per unit time), C is the specific heat (per unit mass) of the gas, T_t is the target temperature, T_n is the nozzle temperature, and e is the efficiency of the gas stream for cooling the target. Equating these, the target temperature is found to be

$$T_t = T_n + \frac{4\pi r^2 \sigma T_r^4 \epsilon}{feC} \quad . \tag{1}$$

Although it assumes equal flows and temperatures for the two nozzles, this equation is readily generalized to the case of unequal values of these parameters. To use Eq. (1), we must first obtain the ratio e/ϵ, other quantities here being known. This is done by obtaining a series of points for which the target is at the triple point[17] of DT, 19.8°K. For each setting of the flow controllers (equal flows from the two nozzles were used), the mean nozzle temperature was found that would just solidify or just melt the fuel. (These were slightly different temperatures; both are plotted.) The temperature variation was achieved by heating the copper rod supporting the nozzle assembly, so that the two nozzle temperatures were nearly equal. The data, plotted in Fig. 40.22, may be fit with a straight line by rewriting Eq. (1) as an expression for T_n. The ratio e/ϵ is then found from the slope of the line to be 0.035 for the particular nozzle assembly and target used in this measurement. It should be noted that the line intersects the vertical axis at the temperature of the target, implying that the nozzles are at the measured temperatures and there is no significant heating of the nozzles by radiation or by conduction through the gas in the chamber. Having determined the ratio e/ϵ, it is reasonable to use a generalized form of Eq. (1) to estimate the target temperature for other combinations of flow and nozzle temperature.

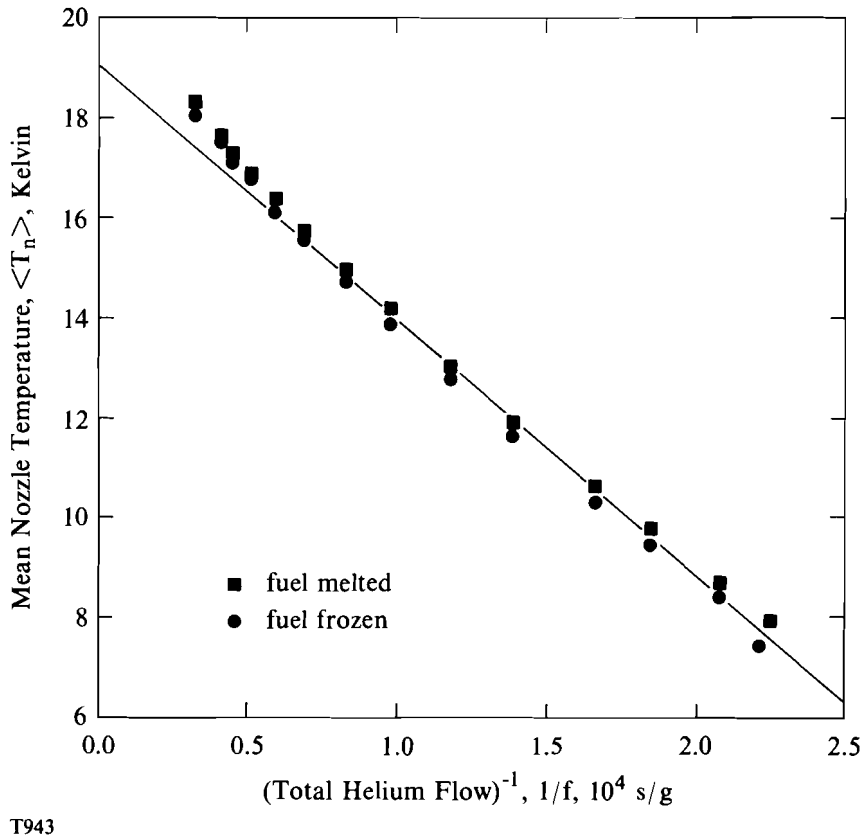

Fig. 40.22
Mean nozzle temperature required to freeze the DT fuel and to remelt the fuel as a function of f^{-1}. The solid line is a fit of Eq. (1) to the data giving most weight to the lower values of flow, which are used for obtaining uniform fuel layers. The intercept to the vertical axis is within the 1°K uncertainty in the thermometer calibration of equaling the 19.8°K triple point of DT. The slope of the line indicates e/ϵ = 0.035. The 251-μm-diameter target is centered between the nozzles, which are 1.8 mm apart and have an inside diameter of 130 μm.

Fuel uniformity in both views is demonstrated in Fig. 40.23. Uniformity is achieved 270±30 ms after applying increased current to the upper nozzle heater. This time depends upon the exact ambient conditions. The ambient conditions are set up so that a reduction of ~0.2°K in the target temperature would cause the fuel to freeze. Under such conditions, the fraction of fuel condensed when uniformity is achieved is in the range of 95% to 98% as measured by template matching to the tilted-phase interferograms. This percentage can probably be maximized by a strategy of increasing the thermal gradient with no change in the mean target temperature. To implement this strategy, heat to the lower nozzle would be decreased at the same moment that heat to the upper nozzle is increased. The helium gas

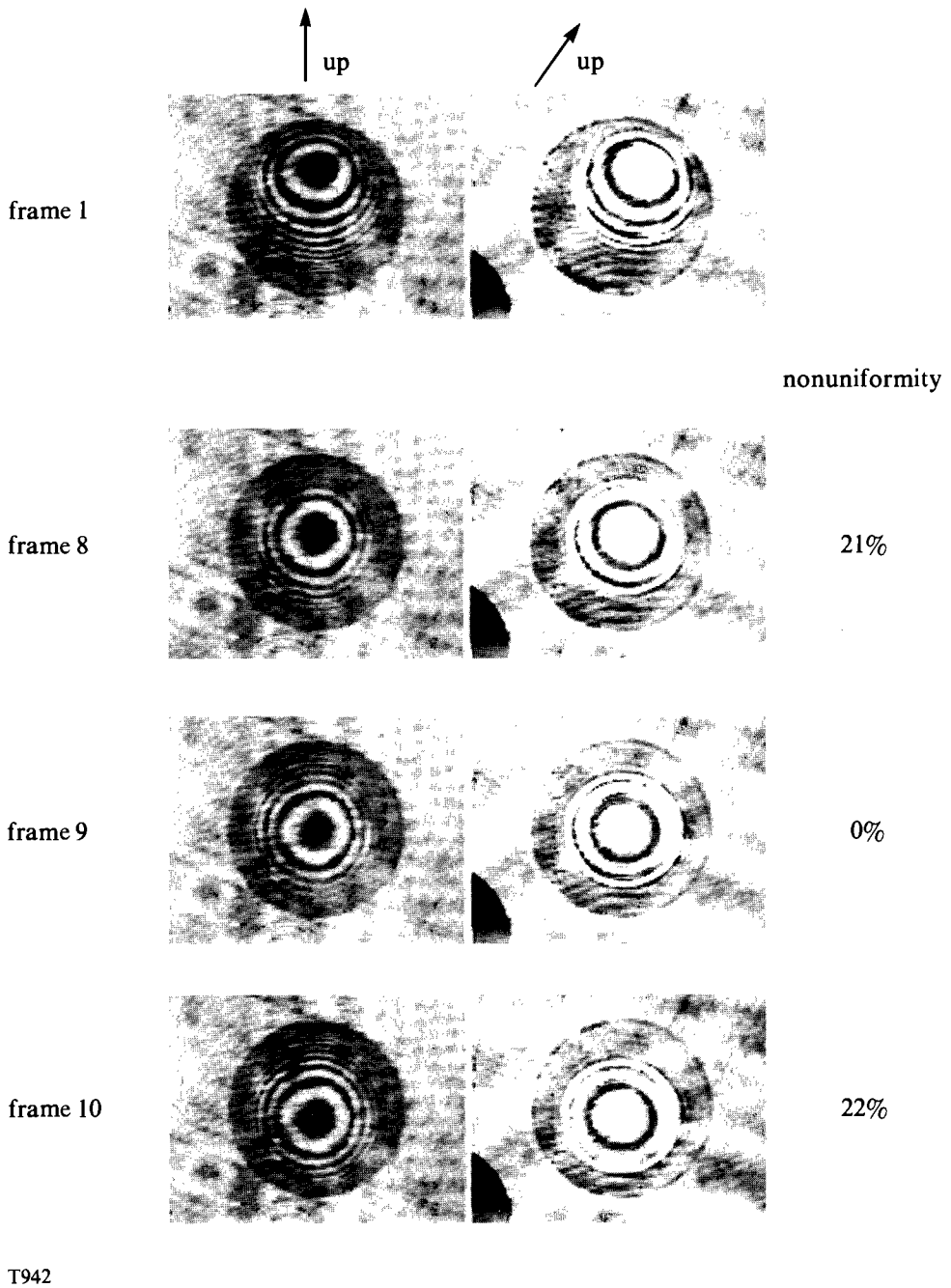

Fig. 40.23
Interferograms demonstrating transient uniformity of the fuel. The left and right images in each pair show the two views, which are at right angles to each other, obtained simultaneously. The upper pair of images show the ambient state before application of the thermal gradient. The three lower pairs of images show sequential video frames, 33 ms apart, as the fuel passes through the state of uniformity. Uniformity is found to occur 270 ± 130 ms after application of the increased thermal gradient.

flow to produce the uniformity seen in Fig. 40.23 was 30 μg/s from each nozzle. This produced a background pressure in the experimental chamber of 0.5 mTorr. The background pressure is dependent upon pumping speed; in this case, a 10-cm diffusion pump was used with a liquid-nitrogen-cooled baffle. It remains to be determined whether the amount of helium gas near the target will interfere with the implosion process. Repeatability of this process to ±30 ms has been demonstrated in these recordings. Efforts will be made to reduce this uncertainty by synchronizing the application of the thermal gradient with the simultaneous recording of the two views.

In conclusion, a transient state of uniformly distributed condensed fuel has been demonstrated in high-pressure DT targets by application of a time-dependent thermal gradient. The technique works in the presence of room-temperature thermal radiation and could be deployed in the target chamber of the OMEGA laser without obstructing any of the beams. A difficulty inherent in this method is the precise adjustment required of the target position with respect to the cold helium gas jets. This method overcomes two difficulties with the instant-refreeze method of obtaining fuel uniformity: it eliminates the need for a retractable isothermal shroud and produces uniformity in targets with much higher pressures than can be made uniform with the instant-refreeze technique. In the process of developing this technique, improved methods of target characterization have been introduced.

ACKNOWLEDGMENT

This work was supported by the U.S. Department of Energy Office of Inertial Fusion under agreement No. DE-FC03-85DP40200 and by the Laser Fusion Feasibility Project at the Laboratory for Laser Energetics, which has the following sponsors: Empire State Electric Energy Research Corporation, New York State Energy Research and Development Authority, Ontario Hydro, and the University of Rochester. Such support does not imply endorsement of the content by any of the above parties.

REFERENCES

1. D. L. Musinski *et al.*, *J. Appl. Phys.* **51**, 1394 (1980).
2. F. J. Marshall, S. A. Letzring, C. P. Verdon, S. Skupsky, R. L. Keck, J. P. Knauer, R. L. Kremens, D. K. Bradley, T. Kessler, J. Delettrez, H. Kim, J. M. Soures, and R. L. McCrory, *Phys. Rev. A.* (to be published).
3. T. Norimatsu *et al.*, *J. Vac. Sci. Technol. A* **6**, 3144 (1988).
4. S. A. Letts *et al.*, *J. Vac. Sci. Technol. A* **6**, 1896 (1988).
5. N. K. Kim, K. Kim, D. A. Payne, and R. S. Upadhye, *J. Vac. Sci. Technol. A* **7**, 1181 (1989).
6. A. J. Martin, R. J. Simms, and R. B. Jacobs, *J. Vac. Sci. Technol. A* **6**, 1885 (1988).
7. J. K. Hoffer and L. R. Foreman, *Phys. Rev. Lett.* **60**, 1310 (1988).
8. K. Kim and D. L. Krahn, *J. Appl. Phys.* **61**, 2729 (1987).

9. V. Varadarajan, K. Kim, and T. P. Bernat, *J. Vac. Sci. Technol. A* **5**, 2750 (1987).

10. L. S. Mok and K. Kim, *J. Fluid Mech.* **176**, 521 (1987).

11. K. Kim, L. Mok, M. J. Erlenborn, and T. P. Bernat, *J. Vac. Sci. Technol. A* **3**, 1196 (1985).

12. K. Kim, B. J. Smoot, R. L. Woerner, and C. D. Hendricks, *Appl. Phys. Lett.* **34**, 282 (1979).

13. S. Denus, W. Muniak, and E. Woryna, *Laser and Particle Beams* **7**, 15 (1989).

14. C. K. Immesoete, L. Forsley, S. Scarantino, and H. Kim, *J. Vac. Sci. Technol.* (to be published).

15. B. A. Brinker, J. M. Cavese, J. R. Miller, S. G. Noyes, S. Sheble, and L. T. Whitaker, *J. Vac. Sci. Technol. A* **1**, 941 (1983).

16. H. Kong, M. D. Wittman, and H. Kim (to be published); see following article [LLE Review **40**, 212 (1989)].

17. P. C. Souers, *Hydrogen Properties for Fusion Energy*, (University of California Press, Berkeley, 1986).

18. G. E. Childs and D. E. Diller, *Adv. Cryo. Eng.* **15**, 65 (1969).

2.C A New Shearing Interferometer for Real-Time Characterization of Cryogenic Laser-Fusion Targets

As discussed in the preceding article, direct-drive inertial confinement fusion targets require a cryogenically cooled spherical shell in which the DT fuel is condensed in a uniform layer on the inner wall. Optical interferometry is the predominant technique used to characterize the thickness and uniformity of the cryogenic fuel layer. In addition to inherent optical limitations such as spherical and chromatic aberration, many of the interferometers used in the past are vibration sensitive or do not possess the adjustment versatility necessary to effectively characterize cryogenic inertial fusion targets. This article describes a new and unique shearing interferometer developed at LLE and implemented on the OMEGA target chamber for real-time characterization of cryogenic inertial fusion targets along two orthogonal views.

The shearing cube interferometer[1] supplied to LLE with the cryogenic target system (developed and built by KMS Fusion) has several limitations. This system uses OMEGA focusing lenses to illuminate and image the fusion target and therefore requires retractable

mirrors to be inserted into the OMEGA beamline during target characterization. Although the interferometer was designed to take advantage of the light-collecting capability of the f/3 OMEGA focusing lenses, the fact that these mirrors must be retracted at least 10 s before the laser shot results in loss of information regarding the state of the target just prior to irradiation. Also, this interferometer analyzes the target only along a single view, which is insufficient to determine the uniformity of the fuel layer in three dimensions. Therefore, it was necessary to develop a dedicated interferometric system that could characterize the state of the target along two orthogonal directions up until a few milliseconds prior to the laser shot.

Several requirements must be met before a type of interferometry can be useful for cryogenic liquid-DT fusion experiments. The portion of the reference wave front used to produce the interferogram must be selectable, and conversion of the background from a constant phase to a high-spatial-frequency fringe pattern must be rapid and reliable. The ability to change between these two states rapidly is essential because a constant phase background is convenient for visual inspection of the overall uniformity and concentricity of the cryogenic DT layer; whereas a high-spatial-frequency fringe pattern is more useful for determining the thickness and local uniformity of the fuel layer.[2] In addition to these properties, the interferogram produced must have high-contrast fringes and the interferometer must be compact enough to be accommodated by the limited space available to a diagnostic on the OMEGA target chamber.

Many types of interferometers have been applied to and developed for investigating the thickness and uniformity of a cryogenic liquid-DT fuel layer condensed on the interior of a laser-fusion target. These interferometers may be classified into two main categories: (1) two-beam interferometry, including ordinary Mach-Zehnder interferometry[3,4] and holographic interferometry,[5–7] and (2) single-beam interferometry, such as rotational-shearing interferometry,[8] lateral-shearing interferometry[9] and wedge interferometry.[10] Two-beam interferometry is difficult to implement on the large scale required by fusion experiments because of its sensitivity to relative vibrations between the two beams. In addition to its extreme sensitivity to vibration, holographic interferometry has the disadvantage of not being a true real-time technique and registration of the hologram and the object under investigation must be precise and reproducible. Both lateral- and rotational-shearing interferometry are limited in that only a relatively small region of the reference wave front can be selected for interference, and their images contain distortion and spherical aberration due to the thick optical plates that must be inserted into the beam path, such as Dove-prisms or shearing cubes. Also, it is difficult to change the interferogram from a constant-phase background to one with high-spatial-frequency interference fringes. Finally, a wedge interferometer is limited by a nonselectable reference wave front and a background-fringe spatial frequency that is fixed by the wedge angle.

Upon realizing the limitations of existing interferometric methods with regard to our application, we sought to develop an alternative

interferometer. One desirable aspect of a shearing interferometer is that both the object and reference wave fronts traverse nearly the same optical path, making it virtually insensitive to vibration and air turbulence. A major asset of a Mach-Zehnder interferometer is that the reference wave fronts are truly plane parallel and their direction of propagation can be widely adjusted in angle with respect to that of the object wave fronts. By combining the desirable features of these two interferometers and eliminating their drawbacks, we have developed a new, compact, single-beam interferometric system that is less sensitive to environmental vibration than a two-beam system; has the ability to select a reference wave front and to change the background fringe frequency from zero to a high value; and has no distortion, chromatic, or spherical aberration. Also, it produces a high-contrast interferogram even with comparatively low target illumination—an important aspect in reducing the heat load on the cryogenic DT fuel.

The entire optical system consists of three subassemblies: (1) an input system to expand and collimate the laser light, (2) an optical-relay system to image the target remotely, and (3) the interferometer itself. A schematic of this system is shown in Fig. 40.24(a). The output beam from an Ar^+ laser (514 nm) is coupled to a single-mode optical fiber that acts as a spatial filter and allows the light to be easily transported to the wall of the OMEGA target chamber. The output end of the fiber is mounted on a multi-axis positioner such that it can be

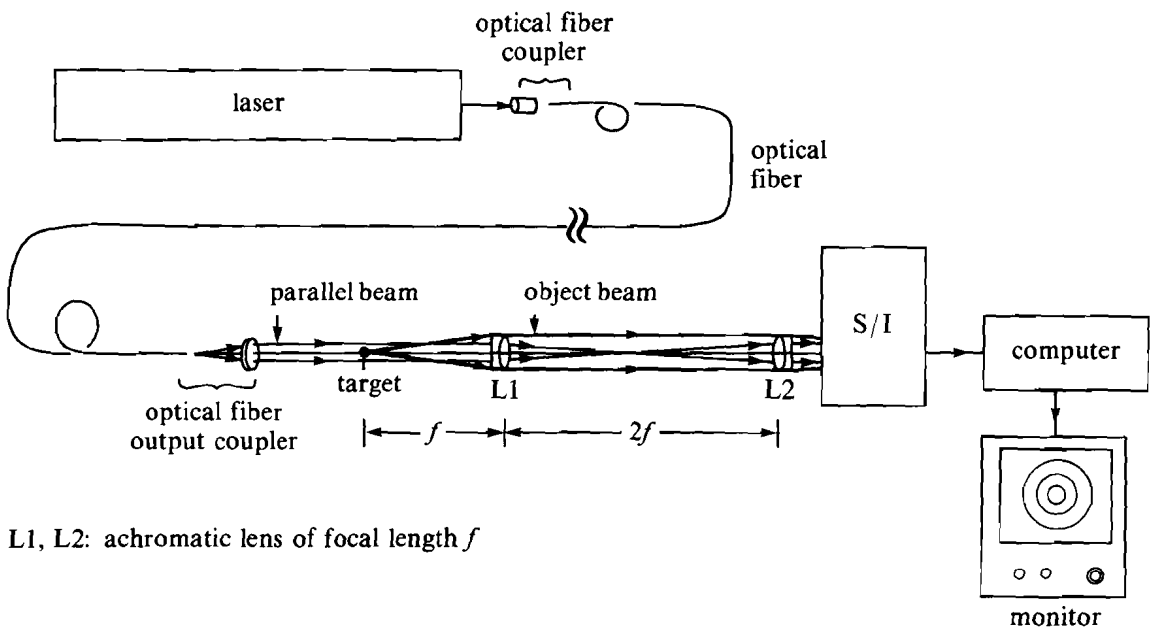

Fig. 40.24(a)
Schematic diagram of the new shearing-interferometer optical system.

positioned with respect to a collimating lens for precise centering, pointing, and collimation of the filtered and expanded laser beam. The input assembly fits compactly onto a vacuum flange used to cover a 4-in. port on the OMEGA target chamber, and the lens itself serves as the vacuum window.

An optical-relay system is used to form an image of the target with a unity magnification. The resultant image is then magnified with a microscope objective lens (20×) onto a high-resolution CCD camera consisting of a 512 × 512 pixel array. The f/5.6 achromatic positive lenses used in the optical-relay system produce a theoretical resolution limit of 3.3 μm. Due to the finite pixel size, the camera approaches the resolution limit of the optical system when the field of view of the magnified image is about 1500 μm. The target image is focused by adjusting the position of the microscope objective lens, and the magnification of the image is controlled by the spacing between the microscope objective lens and the CCD array.

The output assembly, which houses the optical-relay system and supports the interferometer, was also designed around the space requirements of an OMEGA 4-in. port and the solid-angle constraints associated with it. It consists of a vacuum flange with provisions for rigidly mounting the interferometer base plate and a cylindrical tube that extends into the vacuum chamber. The axis of this tube defines the optical axis of the relay system and points directly at the target position at the center of the tank. The lenses are fixed at the desired spacing within the tube using machined shoulders and threaded retaining rings; and the lens farthest from the target also serves as the vacuum window. This feature eliminates the spherical aberration associated with converging or diverging wave fronts passing through a conventional parallel-plate vacuum window.

As shown in Fig. 40.24(b), the interferometer is placed between the optical-relay system and the microscope objective lens. At this position, the portion of the wave front that did not interact with the target is again collimated and the wave front that contains the phase information due to its passage through the target is converging to a focus in front of the microscope objective. The passage of light through the interferometer is as follows: The light emerging from the optical-relay system is split 50/50 in amplitude. The reflected beam from the beam-splitter surface that is reflected again by mirror *M*1 and the transmitted beam through the beam splitter that is reflected by mirror *M*2 are designated by *wf*-1 and *wf*-2 respectively. Each of these two wave fronts is composed of a plane-parallel wave front and the phase information of the target. *Wf*-1 undergoes only first-surface reflections as it passes through the interferometer, so that it is aberration-free upon interacting with its optical components. *Wf*-2 is transmitted twice through the beam splitter so that its image wave front is distorted; however, its plane-parallel component is aberration-free because the plane wave fronts are not distorted by the parallel plate.

The tilt and phase control of the interferometer is done by adjusting *M*2 only; therefore, one can obtain or select the desired interferogram

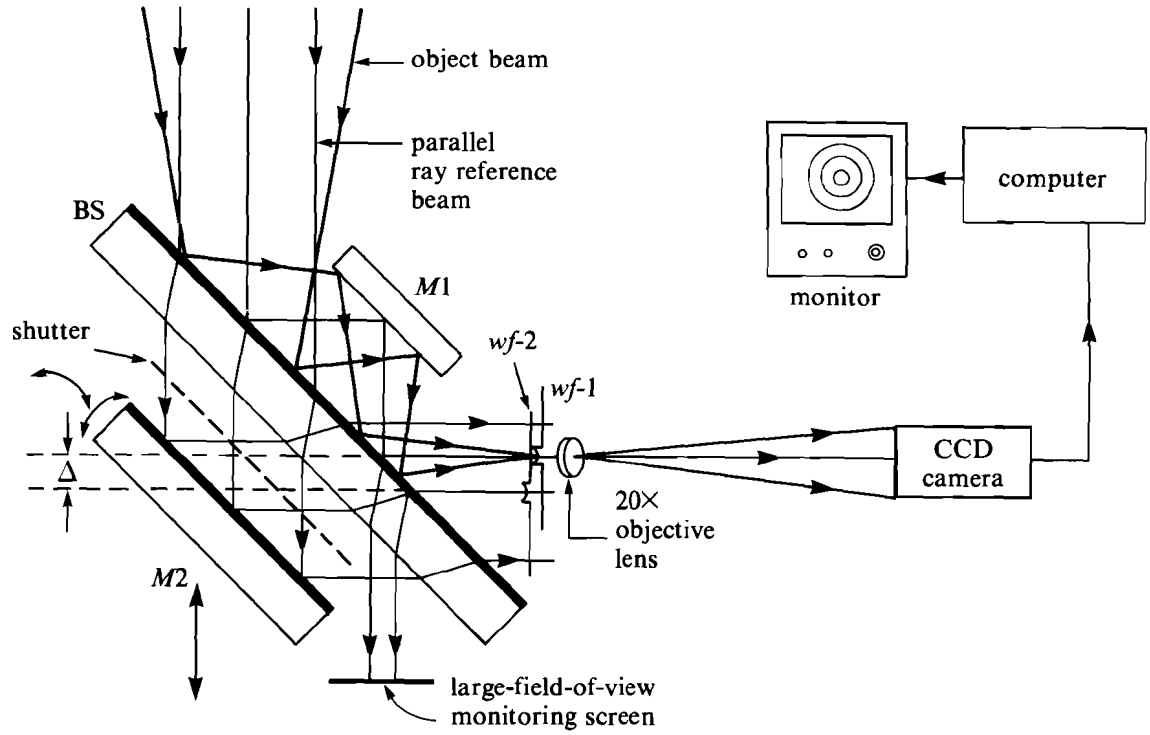

Fig. 40.24(b)
Detailed schematic diagram of the shearing interferometer showing the passage of the object and reference wave fronts through it.

without further alignment of the optical system by repositioning or refocusing the image. This mirror can be rotated about two orthogonal axes that allow the tilt fringes to be oriented along any direction and adjusted continuously in spatial frequency from 0-2000 lines/mm, and also allows one to obtain a very accurate constant background-phase interferogram with a tilt angle $\theta_t < 25$ μrad ($\lambda/40$). This highly accurate alignment is accomplished by using the large-field-of-view interferogram produced by reflection at the beam-splitter surface where *wf*-1 and *wf*-2 recombine as shown in Fig. 40.24(b). Phase control is accomplished by translating *M*2 with respect to the beam-splitter surface; and the minimum phase control is $<\lambda/20$ using a differential micrometer. This phase control allows the precise positioning of the tilt fringes or selection of the background phase when tilt is absent from the interferogram. Selection of the reference wave front is also one dimensionally possible by translating *M*2 by an amount Δ as shown in Fig. 40.24(b) ($0 \leq |\Delta| < 20$ mm). The fact that this is a single-beam interferometer and one that possesses the ability to select a portion of the reference beam that passes near the target to form the interferogram greatly reduces the effects of vibration, air turbulence, and imperfections in the optics that would normally tend to degrade the image.

Figure 40.25(a) shows *wf*-1 and *wf*-2 interfering with each other at the focal point of the optical-relay system. While *wf*-1 is aberration-free, *wf*-2 contains a distorted image but possesses an otherwise aberration-free plane-parallel wave front. Interference fringes appear where the optical path differs by integral multiples of the wavelength used (λ_o) as shown in Fig. 40.25(a). Figures 40.25(b) and 40.25(c) are interferograms obtained when the tilt angle (θ_t) is zero and nonzero respectively. The bull's-eye pattern [Fig. 40.25(b)] is useful for visual inspection of the target uniformity and concentricity, whereas the high-spatial-frequency background pattern [Fig. 40.25(c)] is more suited for detailed two-dimensional calculations of the target's fuel-layer thickness. If a shutter is placed between the beam splitter and mirror *M2*, thus blocking the reference beam, the object beam alone can be imaged, as shown in Fig. 40.25(d). This shadowgram is mainly used for sharply focusing the image onto the CCD detector and positioning it in the field of view, but it can also be used for roughly determining the uniformity and concentricity of the fuel layer. To convert from one type of image to another takes only a few seconds. All of the images have clear outer boundaries, which indicates that they are aberration-free. Each image has a dark band in its outer region that is due to the vignetting effect of the limited aperture size of the f/5.6 optical-relay system.

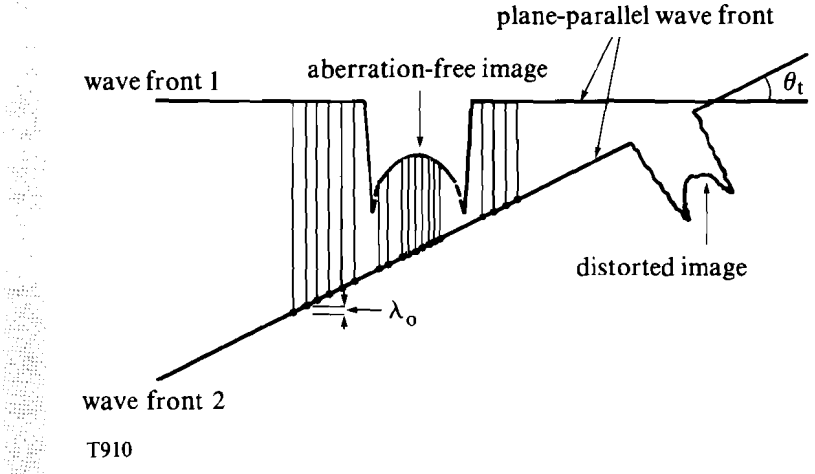

Fig. 40.25(a)
Interference of the object and reference wave fronts at the focal point of the optical-relay system. The parallel lines indicate where the fringes would appear.

In conclusion, we have developed a shearing interferometer that produces an aberration-free interferogram. The interferometer is achromatic, which is essential for obtaining interferograms of several different wavelengths to determine the DT-layer thickness and fractional condensation of the fuel. Two shearing interferometers have been implemented on the target chamber of the OMEGA laser system

to provide orthogonal views of the cryogenic target during experiments. Both of the interferometers can be focused remotely and have remotely controlled shadowgram shutters. The tilt and phase adjustment of one of the interferometers can also be remotely controlled.

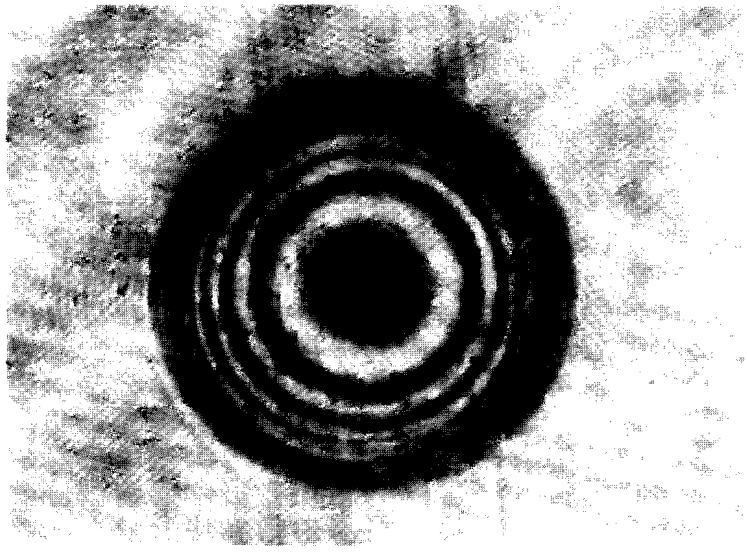

T911

Fig. 40.25(b)
Interferogram of a cryogenic liquid-layer inertial-fusion target using a constant background phase ("bull's-eye" pattern). The glass microballoon has an outer diameter of 262 μm and a wall thickness of 3.8 μm. It contains an equimolar ratio of deuterium and tritium and was filled to a room-temperature pressure of 100 atm.

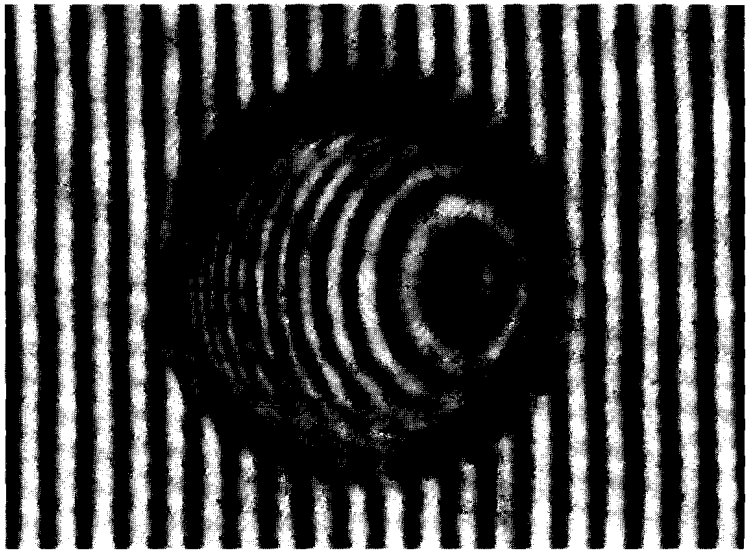

T912

Fig. 40.25(c)
Interferogram of the same target with a high-spatial-frequency background-fringe pattern.

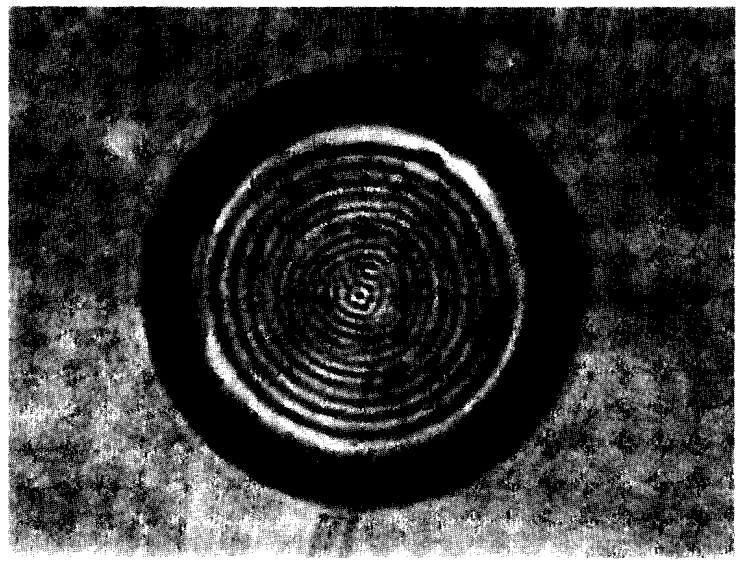

T913

Fig. 40.25(d)
Shadowgram of the same target produced by blocking the reference wave front. The rings appearing inside the image are believed to be due to Fresnel diffraction.

ACKNOWLEDGMENT

This work was supported by the the U.S. Department of Energy Office of Inertial Fusion under agreement No. DE-FC03-85DP40200 and by the Laser Fusion Feasibility Project at the Laboratory for Laser Energetics, which has the following sponsors: Empire State Electric Energy Research Corporation, New York State Energy Research and Development Authority, Ontario Hydro, and the University of Rochester. Partial support by the U.S. Department of Energy under agreement No. DE-AS08-99DP10782 is also acknowledged. Such support does not imply endorsement of the content by any of the above parties.

REFERENCES

1. D. L. Musinski *et al.*, *J. Vac. Sci. Technol. A* **5**, 2746 (1987).
2. LLE Review **31**, 114 (1987).
3. K. Kim, L. Mok, M. J. Erlenborn, and T. P. Bernat, *J. Vac. Sci. Technol. A* **3**, 1196 (1985).
4. K. Kim and D. L. Krahn, *J. Appl. Phys.* **61**, 2729 (1987).
5. T. P. Bernat, D. H. Darling, and J. J. Sanchez, *J. Vac. Sci. Technol.* **20**, 1362 (1982).
6. V. M. Izgorodin, S. B. Kormer, G. P. Nikolaev, and A. V. Pinegin, *Sov. J. Quantum Electron.* **16**, 35 (1986).
7. T. R. Pattinson and W. J. Felmlee, *J. Vac. Sci. Technol. A* **6**, 1882 (1988).
8. T. F. Powers and J. R. Miller, *J. Vac. Sci. Technol. A* **1**, 945 (1983).
9. J. A. Tarvin *et al.*, *Proc. SPIE* **192**, 239 (1979).
10. J. R. Miller and J. E. Sollid, *Appl. Opt.* **17**, 852 (1978).

Section 3
NATIONAL LASER USERS FACILITY NEWS

During the fourth quarter of FY89 there were three NLUF activities: a visit by **C. F. Hooper** of the University of Florida to plan for future target shots on OMEGA; a series of GDL experiments conducted by **K. Mizuno** from **J. DeGroot's** group at the University of California at Davis (UCD); and a meeting of the NLUF Steering Committee to review FY90 proposals.

C. F. Hooper is collaborating with the LLE staff in conducting a series of implosions of argon-filled plastic shells. Two series of experiments are planned: The first will use a set of targets that duplicate those shot during December 1987. These targets were filled with pure Ar at varying pressures. Results from these implosions have been published in *Physical Review Letters*. The second set of targets will use the Ar as a seed gas in D_2-filled plastic shells. Different mixtures of Ar and D_2 will be used, and spectra of the Ar ions will be measured. The added data from the Ar spectra should give more information about the core conditions of the D_2 implosion.

J. DeGroot's group has been collaborating with **W. Seka** of LLE to measure plasma instabilities associated with the laser irradiation of solid targets. The primary objective of this experiment is to measure the ion acoustic decay instability (IADI) for targets of various atomic numbers. This is a continuation of work done at UCD with microwave sources and at LLE with GDL. Recent shots at LLE have studied the atomic-number dependence of the IADI over a larger range of

irradiation conditions. The data are to be analyzed at UCD and LLE and a series of experiments on the OMEGA laser system is in the planning stage.

The NLUF Steering Committee met on 18 July 1989. In attendance were **Dean B. Arden**, University of Rochester; **Dr. J. Knauer**, University of Rochester; **Mr. G. D'Alessio**, Department of Energy; **Dr. K. Hill**, Princeton Plasma Physics Laboratory; **Dr. W. Kruer**, Lawrence Livermore National Laboratory; **Dr. K. Matzen**, Sandia National Laboratory; **Dr. D. Nagel**, Naval Research Laboratory; **Dr. J. Perez**, University of Auburn; and **Dr. E. Spiller**, IBM Watson Research Laboratory.

Ten proposals for FY90 were reviewed by the committee, and recommendations were then passed on to the DOE San Francisco office, where final decisions on funding were made and principal investigators were notified. Funding for FY90 is expected to remain at $600,000, implying that only a few of the proposals can be accepted.

The following proposals were submitted for FY90:

1. X-Ray Contact Microradiography and Shadow Projection Microscopy Using a Laser-Produced Plasma;
2. Fusion with Highly Spin-Polarized HD and D_2;
3. A New Diagnostic Technique to Simultaneously Measure the Electron Temperature, Ionic Charge State, and Plasma Density near the Critical Surface in Laser-Plasma Interaction Experiments;
4. Time-Resolved Extreme-Ultraviolet Spectroscopy of Laser-Produced Plasmas Originating at the Parylene Layer of Microballoon Targets;
5. Time-Resolved Emission and Absorption Spectroscopy of Laser-Driven Implosions;
6. Induction of ICF with Diffraction-Free Laser Beams;
7. Laser Shock Deformation and Microstructural Modification of Metals;
8. X-Ray Crystal Devices for Measuring Compression and Stability of Laser Fusion Targets;
9. A Time-Dependent Study of the Ionization Dynamics in a Laser-Produced Plasma from a Supersonic Gas Jet; and
10. XUV Spectroscopic Studies at the OMEGA Laser.

ACKNOWLEDGMENT

This work was supported by the U.S. Department of Energy Office of Inertial Fusion under agreement No. DE-FC03-85DP40200.

Section 4
LASER SYSTEM REPORT

4.A GDL Facility Report

During the fourth quarter of FY89, the highlight of the experimental program was the observation of soft x-ray lasing at 195 Å, 232 Å, and 236 Å. The lasing was produced by irradiating a germanium foil with a 15-mm-long line focus from the GDL laser. Neon-like germanium ions, which were collisionally excited by plasma electrons, provided the gain medium. Additional programs on GDL included the continuation of the shine-through experiments, the deployment of the short-pulse (~20-ps) probe beam in the Beta chamber, and a Thomson-scattering experiment. The shine-through experiments continued investigation of early-time phenomena in laser-produced plasmas, in particular the transmission of light through a target before the generation of a plasma. The probe beam that has been directed to the GDL target-irradiation facility will be used in two manners: first, as a backlight source (527 nm) for an imaging system that will investigate plasma generation and expansion; second, as a pump beam for Thomson-scattering experiments.

One NLUF user experiment, measurement of the ion-acoustic decay instability, by a group from the University of California at Davis (UCD) was conducted for an entire week.

A summary of the GDL operation follows:

Beamline Test, Calibration, Tuning, and Laser Alignment Shots	150
Target Shots	
Shine-through	52
X-Ray Laser	42
X-Ray Lithography	13
Probe Beam/Thomson Scattering	21
NLUF (UCD)	53
TOTAL	331

ACKNOWLEDGMENT

This work was supported by the U.S. Department of Energy Office of Inertial Fusion under agreement No. DE-FC03-85DP40200 and by the Laser Fusion Feasibility Project at the Laboratory for Laser Energetics, which has the following sponsors: Empire State Electric Energy Research Corporation, New York State Energy Research and Development Authority, Ontario Hydro, and the University of Rochester. Such support does not imply endorsement of the content by any of the above parties.

4.B OMEGA Facility Report

The final quarter in FY89 began with a thorough analysis of the state of power balance among the 24 OMEGA laser beams. A theoretical analysis was conducted using the MALAPROP laser-propagation code that determined the relationship between temporal pulse shape and system gain. A rather strong dependence of pulse shape on gain dictated that the gains of each of the 24 chains be equalized. In addition to adding amplifier small-signal-gain-measurement capability, the electrical-energy storage banks were converted to adjustable energy. Along with these significant power-balance improvements, there were newly developed smoothing by spectral dispersion (SSD) upgrades implemented and testing of them has begun on OMEGA.

A flip-in photodiode system, in conjunction with the OMEGA oscillator, is used to measure the optical gains of all amplifiers to within $\pm 2\%$ in a three-hour experiment. Results of these tests indicated some reduction in amplifier gain between maintenance operations. As amplifier modules were refurbished, the gain variation was reduced and large imbalances eliminated. Fine tuning to achieve exact gain equalization required control over the electrical pump source. This resulted in $\sim 2\%$-rms gain variations among the 24 beamlines.

A synopsis of laser shots for this quarter follows:

Software Test	68
Driver Line	86
Laser	280
Target	101
TOTAL	535

ACKNOWLEDGMENT

This work was supported by the U.S. Department of Energy Office of Inertial Fusion under agreement No. DE-FC03-85DP40200 and by the Laser Fusion Feasibility Project at the Laboratory for Laser Energetics, which has the following sponsors: Empire State Electric Energy Research Corporation, New York State Energy Research and Development Authority, Ontario Hydro, and the University of Rochester. Such support does not imply endorsement of the content by any of the above parties.

PUBLICATIONS AND CONFERENCE PRESENTATIONS

Publications

W. R. Donaldson, "Picosecond and Femtosecond Laser Systems for Particle Accelerator Applications," in *Proceedings of the Switched Power Workshop*, edited by R. C. Fernow (Brookhaven National Laboratory, New York, 1989), pp. 191–219.

J. H. Kelly, M. J. Shoup III, and D. L. Smith, "OMEGA Upgrade Staging Options," *High Power and Solid State Lasers II* (SPIE, Bellingham, WA, 1989), Vol. 1040, pp. 184–190.

C. J. McKinstrie and J. M. Kindel, "Laser-Plasma Acceleration of Particles," in *Laser-Induced Plasmas and Applications*, edited by L. J. Radziemski and D. A. Cremers (Dekker, New York, 1989), p. 413.

T. B. Norris, N. Vodjdani, B. Vinter, C. Weisbuch, and G. A. Mourou, "Charge-Transfer State Photoluminescence in Asymmetric Coupled Quantum Wells," *Phys. Rev. B* **40**, 1392–1395 (1989).

C. F. Hooper, Jr., D. P. Kilcrease, R. C. Mancini, L. A. Woltz, D. K. Bradley, P. A. Jaanimagi, and M. C. Richardson, "Time-Resolved Spectroscopic Measurements of High Density in Ar-Filled Microballoon Implosions," *Phys. Rev. Lett.* **63**, 267–270 (1989).

S. Krishnamurthy and S. H. Chen, "Purification of Thermotropic Liquid Crystalline Siloxane Oligomer with Supercritical Carbon Dioxide," *Makromol. Chem.* **190**, 1407–1412 (1989).

Forthcoming Publications

T. Boehly, B. Yaakobi, D. Shvarts, D. Meyerhofer, P. Audebert, J. Wang, M. Russotto, B. Boswell, R. Epstein, R. S. Craxton, and J. M. Soures, "X-Ray Laser Experiments Using Double Foil Nickel Targets," to be published in *Applied Physics B.*

B. Boswell, D. Shvarts, T. Boehly, and B. Yaakobi, "X-Ray Laser Beam Propagation in Double-Foil Targets," to be published in *Physics of Fluids.*

J. M. Chwalek, D. R. Dykaar, J. F. Whitaker, R. Sobolewski, S. Gupta, T. Y. Hsiang, and G. A. Mourou, "Ultrafast Response of Superconducting Transmission Lines," to be published in *Ultrafast Phenomena VI.*

J. M. Chwalek, D. R. Dykaar, J. F. Whitaker, T. Y. Hsiang, G. A. Mourou, D. K. Lathrop, S. E. Russek, and R. A. Buhrman, "Picosecond Transient Propagation Studies on Thin-Film Y-Ba-Cu-O Transmission Lines," to be published in *Ultrafast Phenomena VI.*

W. R. Donaldson, A. M. Kadin, P. H. Ballentine, and M. Shoup III, "Optically Activated High Temperature Superconductor Opening Switches," to be published in the *Proceedings of the 7th IEEE Pulsed Power Conference*, Monterey, CA, 11–14 June 1989.

D. R. Dykaar, R. Sobolewski, and T. Y. Hsiang, "Picosecond Switching Dynamics of a Josephson Tunnel Junction," to be published in *Ultrafast Phenomena VI.*

M. Y. Frankel and T. Y. Hsiang, "Picosecond Transient Behavior of Pseudomorphic High Electron Mobility Transistor–Simulations," to be published in *IEEE Transactions on Electron Devices.*

M. Y. Frankel, D. R. Dykaar, T. Y. Hsiang, K. H. Duh, and P. C. Chao, "Non-Invasive, Picosecond Transient Characterization of Pseudomorphic High Electron Mobility Transistor (HEMT)," to be published in *IEEE Transactions on Electron Devices.*

T. Y. Hsiang, J. F. Whitaker, R. Sobolewski, S. Martinet, and L. P. Golob, "High-Frequency Characterization of Superconducting Transmission Structures from Picosecond Transient Measurements," to be published in the *Proceedings of the 1989 International Superconductive Electronics Conference (SEEC '89)*, Tokyo, Japan, 13 June 1989.

C. Immesoete, L. Forsley, and H. Kim, "Computer-Assisted Microballoon Selection for Laser Fusion Targets," to be published in the *Proceedings of the Forth Conference,* Rochester, NY, 19–23 June 1989.

S. D. Jacobs, "Better Lasers From Better Materials," to be published in *CHEMTECH* (invited article).

H. G. Kim, P. C. Cheng, M. D. Wittman, and H. J. Kong, "X-Ray Microscopy of Living Biological Specimens Using a Laser Plasma as an

X-Ray Source," to be published in the *Proceedings of the International Congress on Optical Science and Engineering Conference*, Paris, France, 24–28 April 1989.

H. G. Kim, P. C. Cheng, M. D. Wittman, and H. J. Kong, "Pulsed X-Ray Contact Microradiography and its Applications to Structural and Developmental Botany," to be published as a book chapter in *Tochigi Meeting in X-Ray Microscopy 88.*

P. Maine, D. Strickland, M. Pessot, J. Squier, P. Bado, G. Mourou, and D. Harter, "Chirped Pulse Amplification: Present and Future," to be published in *Ultrafast Phenomena VI.*

F. J. Marshall, S. A. Letzring, C. P. Verdon, R. L. Kremens, S. Skupsky, R. L. Keck, J. P. Knauer, D. K. Bradley, T. Kessler, J. A. Delettrez, H. Kim, J. M. Soures, and R. L. McCrory, "Cryogenic-Laser-Fusion-Target Implosion Studies Performed with the OMEGA UV Laser System," to be published in *Physical Review A.*

R. L. McCrory, "Energy Supply and Demand in the Twenty-First Century," to be published in *Journal of Fusion Energy.*

R. L. McCrory, "Progress and Plans for Inertial Confinement Fusion at the University of Rochester," to be published in *Journal of Fusion Energy.*

R. L. McCrory and C. P. Verdon, "Computer Modeling and Simulation in Inertial Confinement Fusion," to be published in *Il Nuovo Cimento.*

R. L. McCrory, J. M. Soures, C. P. Verdon, S. Skupsky, T. J. Kessler, S. A. Letzring, W. Seka, R. S. Craxton, R. Short, P. A. Jaanimagi, M. Skeldon, D. K. Bradley, J. Delettrez, R. L. Keck, H. Kim, J. P. Knauer, R. L. Kremens, and F. J. Marshall, "Laser Compression and Stability in Inertial Confinement Fusion," to be published in *Plasma Physics and Controlled Fusion.*

C. J. McKinstrie and G. G. Luther, "The Modulational Instability of Colinear Waves," to be published in *Physica Scripta, Special Issue on Large-Amplitude Waves in Plasmas.*

T. B. Norris, N. Vodjdani, B. Vinter, C. Weisbuch, and G. A. Mourou, "Time-Resolved Observation of Luminescence from a Charge-Transfer State in Double Quantum Wells," to be published in the *Proceedings of the Optical Society of America, Quantum Wells for Optics and Optoelectronics*, Salt Lake City, UT, 6–8 March 1989.

T. B. Norris, X. J. Song, G. Wicks, W. J. Schaff, L. F. Eastman, and G. A. Mourou, "Electric Field Dependence of the Tunneling Escape Time of Electrons from a Quantum Well," to be published in the *Proceedings of Picosecond Electronics and Optoelectronics Conference*, Salt Lake City, UT, 8–10 March 1989.

M. Pessot, J. Squier, G. Mourou, and D. J. Harter, "Chirped Pulse Amplification of 100 fs Pulses," to be published in *Optics Letters.*

M. Pessot, J. Squier, G. Mourou, and D. J. Harter, "Amplification of 100 fsec mJ Pulses in Alexandrite Using Chirped Pulse Techniques," to be published in the *Proceedings of Tunable Solid State Laser Meeting*, Cape Cod, MA, 1–3 May 1989.

S. Skupsky, R. W. Short, T. Kessler, R. S. Craxton, S. Letzring, and J. M. Soures, "Improved Laser-Beam Uniformity Using the Angular Dispersion of Frequency-Modulated Light," to be published in *Journal of Applied Physics*.

D. L. Smith, J. H. Kelly, and M. J. Shoup, "A Low Cost Active-Active Oscillator Utilizing Loss Feedback Control," to be published in *Applied Optics*.

J. M. Soures, "Remarks of J. M. Soures at the Fusion Power Associates Panel Discussion," to be published in *Journal of Fusion Energy*.

J. F. Whitaker, T. B. Norris, G. Mourou, T. C. Sollner, W. D. Goodhue, X. J. Song, and L. F. Eastman, "Tunneling-Time Measurements of a Resonant Tunneling Diode," to be published in *Ultrafast Phenomena VI*.

P. C. Cheng, V. H-K. Chen, H. G. Kim, and R. E. Pearson, "A Real-Time EPI-Fluorescent Confocal Microscope," to be published in *Journal of Microscopy*.

P. C. Cheng, V. H-K. Chen, H. G. Kim, and R. E. Pearson, "An EPI-Fluorescent Spinning-Disk Confocal Microscope," to be published in the *Proceedings of the 47th Annual Meeting of Electron Microscopy Society of America (EMSA)*, Austin, TX, 14–18 August 1989.

A. M. Kadin, W. R. Donaldson, P. H. Ballentine, and R. Sobolewski, "Nonequilibrium Hot-Electron Transport in Optically Irradiated YBCO Films," to be published in *PHYSICA-C, Special Issue, Proceedings of the International M2S-HTSC Conference*, Stanford, CA, 23–28 July 1989.

H. J. Kong, M. D. Wittman, and H. G. Kim, "A New Shearing Interferometer for Real-Time Characterization of Cryogenic Laser Fusion Targets," to be published in *Applied Physics Letters*.

J. C. Lambropoulos, "Analysis of Thermal Stress, Fracture and Strengthening by Ion Exchange in Glass for High Average Power Laser Applications," to be published in *Journal of Applied Physics*.

J. C. Lambropoulos, M. R. Jolly, C. A. Amsden, S. E. Gilman, M. J. Sinicropi, D. Diakomihalis, and S. D. Jacobs, "Thermal Conductivity of Dielectric Thin Films," to be published in *Journal of Applied Physics*.

F. W. Smith, S. Gupta, H. Q. Le, M. Frankel, V. Diadiuk, M. A. Hollis, D. R. Dykaar, G. A. Mourou, T. Y. Hsiang, and A. R. Calawa, "Picosecond GaAs-Based Photoconductive Optoelectronic Detectors," to be published in *Applied Physics Letters*.

M. L. Tsai and S. H. Chen, "Helical Sense in Thermotropic Liquid Crystal Copolymers in Relation to the Structure of Pendant Chiral Moiety," to be published in *Macromolecules*.

M. L. Tsai, S. H. Chen, K. L. Marshall, and S. D. Jacobs, "Thermotropic and Optical Properties of Chiral Nematic Polymers," to be published in *International Journal of Thermophysics*.

X. Zhou and T. Y. Hsiang, "Monte Carlo Study of Photo-Generated Carrier Transport in GaAs Surface Space Charge Fields," to be published *Journal of Applied Physics*.

Conference Presentations

A. Lindquist, S. D. Jacobs, and V. Plotsker, "Chemo-Mechanical Prepolish of Glass for Reducing Subsurface Damage and Polishing Time," presented at the Conference on Large Optics, Rome, NY, 11–13 July 1989.

A. M. Kadin, W. R. Donaldson, P. H. Ballentine, and R. Sobolewski, "Nonequilibrium Hot-Electron Transport in Optically Irradiated YBCO Films," presented at the International M2S-HTSC Conference, Stanford, CA, 23–28 July 1989.

The following presentations were made at the Botanical Society of America/Canadian Botanical Association Joint Meeting, Toronto, Canada, 6–10 August 1989:

P. C. Cheng and H. G. Kim, "The Use of X-Ray Contact Microradiography in the Study of Silica Deposition in the Leaf Blade of Maize."

P. C. Cheng, V. H. Chen, H. G. Kim, and R. E. Pearson, "Confocal Microscopy and its Applications in Structural and Developmental Botany."

The following presentations were made at the SPIE's 33rd Annual International Symposium, San Diego, CA, 6–11 August 1989:

P. A. Jaanimagi, R. Saunders, C. Hestdalen, W. VanRemmen, and M. Russotto, "Pulse Shape Measurements on OMEGA."

H. G. Kim, and P. C. Cheng, "Pulse X-Ray Contact Microradiography and Real-Time X-Ray Projection Micrography."

The following presentations were made at the Optical Society of America Topical Meeting, Snowbird, UT, 11–13 September 1989:

H. E. Elsayed-Ali, "Hot Electron Relaxation in Metals" (invited paper).

D. D. Meyerhofer, S. Augst, Y-H. Chuang, J. Delettrez, and M. C. Richardson, "Comparison of Multiphoton and Collisional Ionization in High Intensity Laser-Plasma Interactions."

M. C. Richardson, H. Chen, Y-H. Chuang, J. Delettrez, R. Epstein, T. Kessler, D. D. Meyerhofer, S. Uchida, and B. Yaakobi, "High Intensity Picosecond Pulse Interaction Experiments."

The following presentations were made at the Seventh Target Fabrication Specialists' Meeting, Livermore, CA, 25–29 September 1989:

H. G. Kim, R. Q. Gram, M. D. Wittman, C. Immesoete, R. S. Craxton, N. Sampat, S. Swales, G. Pien, and J. M. Soures, "Uniformity of Condensed DT Layers in Gas-Cooled Inertial Fusion Targets."

H. G. Kim, C. Immesoete, and S. Scarantino, "Computer Assisted Microballoon Selection for Inertial Confinement Targets."

H. G. Kim, M. D. Wittman, and J. M. Soures, "A Shearing Interferometer for Real-Time Characterization of Cryogenic Laser Fusion Targets."

J. M. Soures, "Implosion Experiments at LLE" (invited paper).

ACKNOWLEDGMENT

The work described in this volume includes current research at the Laboratory for Laser Energetics, which is supported by Empire State Electric Energy Research Corporation, New York State Energy Research and Development Authority, Ontario Hydro, the University of Rochester, and the U.S. Department of Energy Office of Inertial Fusion under agreement No. DE-FC03-85DP40200.